A non-equilibrium quantum transport framework for spintronic devices with dynamical correlations

Declan Nell, ¹ Milos Radonjic, ² Ivan Rungger, ³ Liviu Chioncel, ⁴ Stefano Sanvito, ¹ and Andrea Droghetti^{1,5,*}

¹ School of Physics and CRANN Institute, Trinity College Dublin, The University of Dublin, Dublin 2, Ireland

² Institute of Physics Belgrade, University of Belgrade, 11000 Belgrade, Serbia

³ National Physical Laboratory, Hampton Road, Teddington TW11 0LW, United Kingdom

⁴ Theoretical Physics III, Center for Electronic Correlations and Magnetism,

Institute of Physics, and Augsburg Center for Innovative Technologies,

University of Augsburg, 86135 Augsburg, Germany

⁵ Department of Molecular Sciences and Nanosystems,

Ca' Foscari University of Venice, via Torino 155, 30170, Mestre-Venice, Italy

Two-terminal spintronic devices remain challenging to model under realistic operating conditions, where the interplay of complex electronic structures, correlation effects and bias-driven nonequilibrium dynamics may significantly impact charge and spin transport. Existing ab initio methods either capture bias-dependent transport but neglect dynamical correlations or include correlations but are restricted to equilibrium or linear-response regimes. To overcome these limitations, we present a framework for steady-state quantum transport, combining density functional theory (DFT), the non-equilibrium Greens' function (NEGF) method, and dynamical mean-field theory (DMFT). The framework is then applied to Cu/Co/vacuum/Cu and an Fe/MgO/Fe tunnel junction. In Co, correlations drive a transition from Fermi-liquid to non-Fermi-liquid behavior under finite bias, due to scattering of electrons with electron-hole pairs. This leads to incoherent contributions to the conductance that are observable in scanning tunneling spectroscopy experiments. In contrast, in the Fe/MgO/Fe junction, correlation effects are weaker: Fe remains close to equilibrium even at large biases. Nevertheless, inelastic scattering can still induce partly incoherent transport that modifies the device's response to the external bias. Overall, our framework provides a route to model spintronic devices beyond single-particle descriptions, while also suggesting new interpretations of experiments.

I. INTRODUCTION

Spintronics exploits spin-dependent transport phenomena in materials, with applications in logic and data storage [1]. Typical devices are heterostructures formed by stacking thin magnetic and non-magnetic layers. Among these, magnetic tunnel junctions (MTJs) [2–5] exhibiting tunneling magnetoresistance (TMR) [6–8] are already standard components in commercial read heads for hard-disk drives. However, the computational description of spintronic devices remains generally challenging due to their complex electronic structure, their open nature — allowing carriers to flow in and out of the active region — and the inherently non-equilibrium character of transport.

Ab initio studies typically rely on Kohn-Sham (KS) Density Functional Theory (DFT) [9–11], within either the Local Spin Density Approximation (LSDA) [12, 13] or the Generalized Gradient Approximation (GGA) [14–16] for the exchange-correlation functional, combined with the Landauer-Büttiker (LB) approach [17–19] to quantum transport. In this framework, a device is treated as a central open region connected to electrodes that act as charge reservoirs, as shown in Fig. 1(a). The spin-dependent conductance is determined by the transmission of spin-polarized KS single-particle states from one

electrode, through the central device region, to the opposite electrode [20]. Practical implementations include transfer-matrix methods [21, 22], layer Korringa-Kohn-Rostoker approaches [23], and mode-matching techniques [24].

The most versatile and widely adopted implementation, however, is based on the non-equilibrium Green's function (NEGF) formalism [25–27] in its steady-state formulation. Commonly referred to as DFT+NEGF [28–30], this method enables the calculation of transport properties at finite bias, going beyond the linear-response regime assumed in the original LB approach. As a result, it provides a device's current-voltage (I-V) characteristics [31–35] as well as other voltage-dependent observables, such as the spin-transfer torque [36–39].

DFT+NEGF relies on the assumption that the KS states provide a reasonable approximation of the excitation spectrum of a system. However, beyond issues of formal consistency [40], this assumption often fails even in practice, particularly for the 3d ferromagnets (Fe, Ni, Co, and related compounds) widely used in spintronic devices. Comparison with photoemission experiments shows that KS-DFT overestimates the spin splitting of the 3d states and produces majority-spin spectra that are too broad. Moreover, it neglects finite-lifetime effects arising from electron-electron interaction, which broaden the electronic bands in both energy and momentum [41, 42]. Finally, the phase-coherent picture of transport in terms of electron transmission may break

 $^{^*}$ andrea.droghetti@unive.it

down due to electron correlation effects. For instance, features observed in MTJs' *I-V* characteristics have been interpreted as signatures of inelastic electron-electron or electron-magnon scattering [43–46]. While such effects can be included phenomenologically in DFT+NEGF, for example via Büttiker probes [47, 48], a truly *ab initio* treatment requires going beyond KS-DFT.

An improved description of the electronic structure of 3d metals can be achieved by combining DFT with Dynamical Mean-Field Theory (DMFT), in the so-called DFT+DMFT method [49–54]. Through the incorporation of dynamic, yet local-in-space, correlations, DMFT corrects the overestimation of spin-splitting and yields spectral properties in closer agreement with experiment [55–59]. Moreover, DMFT provides a true *ab initio* treatment of quasiparticle lifetimes and naturally captures incoherent effects arising from electron-electron scattering.

DMFT can be applied to study transport in devices using a layered formulation [60–67] in the linear-response regime. It can then be combined with DFT for *ab initio* calculations [68–72], building on embedding frameworks originally developed for point contacts [73–75] and molecular junctions [76–82]. The idea is to apply DMFT to a "correlated region", defined within the central device region and hosting significant electron-electron interaction. Recently, these DFT+DMFT implementations for transport have also been generalized to "quasi-equilibrium" conditions [59], valid when the voltage drop, albeit large in the device, remains small within the correlated region.

Genuine non-equilibrium conditions can be tackled by formulating DMFT within the NEGF framework using the Keldysh formalism [83–85]. Existing implementations, however, are typically designed for model bulk systems and focus on transient electron dynamics in the time domain. Studies of steady-state transport at finite bias in a device setup remain scarce and are generally limited to single-orbital models, employing ansätze for the Keldysh component of the many-body self-energy [86, 87], workflows that compute only the retarded self-energy [88], or master-equation solvers [89]. Implementations for non-equilibrium bias-driven transport through realistic materials, described by multiple orbitals per atomic site, are still lacking, leaving electron correlation effects in current-carrying spintronic devices largely unexplored.

In this paper, we present a computational framework combining DFT, DMFT and NEGF in the steady-state regime to study transport properties of devices beyond the linear-response limit or quasi-equilibrium ansätze adopted in previous DFT+DMFT transport implementations [59]. Our approach, that we called DFT+NEGF+DMFT, enables us to capture correlation effects induced by a finite bias, even in systems where a significant portion of the voltage drop occurs within the correlated region, leading to inherently non-equilibrium many-electron behavior.

Our framework is applied to two prototypical systems. The first one consists of a single Co monolayer sandwiched between Cu electrodes, with a gap introduced be-

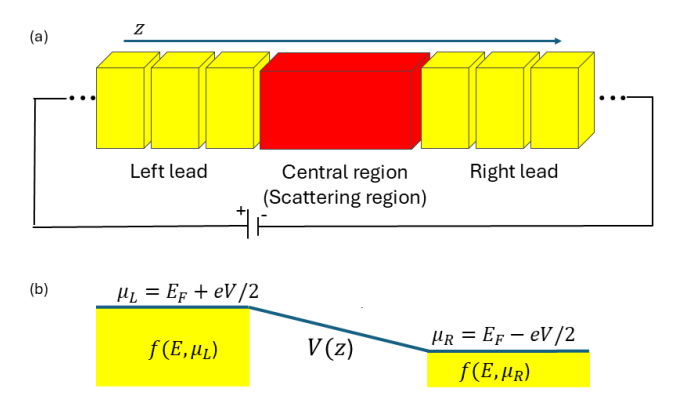


FIG. 1. Schematic illustration of a typical two-terminal transport setup. (a) A two-terminal spintronic device is modelled as infinite along the transport direction and partitioned into a central (scattering) region contacted by semi-infinite metallic leads. (b) Each lead acts as an electronic reservoir. Under a finite bias voltage, V, the leads individually remain in equilibrium, with their electronic states occupied according to the Fermi-Dirac distribution functions, $f_{\rm L(R)}(E,\mu_{\rm L(R)})$, determined by the relative lead chemical potential L(R). The electrostatic potential V(z) drops inside the central region.

tween one electrode and the Co layer to allow for a potential drop under bias. Our results demonstrate that non-equilibrium correlations in Co drive a qualitative transition from Fermi-liquid to non-Fermi-liquid behavior, arising from the inelastic scattering of electrons with collective electron-hole excitations. This reshapes the DFT-KS electronic structure and gives rise to incoherent contributions to the conductance, that can be measured through scanning tunneling spectroscopy (STS).

The second system represents the active part of an Fe/MgO/Fe MTJ. Here, the applied bias is found to have a much weaker effect on Fe, validating the quasi-equilibrium approximations employed in previous studies [59]. Nevertheless, even in this limit, bias-induced inelastic scattering generates incoherent contributions to the current, which impact the device transport properties and performance.

The paper is organized as follows. In Sec. II, we introduce the method and describe its implementation. Computational details are provided in Sec. III. Results are presented in Sec. IV, focusing first on the Co/Cu system in Sec. IV A, and then on the Fe/MgO/Fe MTJ in Sec. IV B. Finally, we draw our conclusions in Sec. V.

II. METHOD AND IMPLEMENTATION

Our framework applies to the standard setup commonly used in quantum transport simulations of two-terminal devices under an applied bias voltage, as described in Sec. II A. It is formulated within the NEGF formalism in the steady-state limit, briefly reviewed in

Sec. IIB, where the relevant notations are defined. The implementation then proceeds through several key steps, as follows.

At the first level, the method relies on DFT+NEGF calculations to provide an effective single-particle description of the device electronic structure, namely a static mean-field treatment under bias. This standard methodology is summarized in Sec. II C. From this starting point, we employ an embedding algorithm to extract a correlated subsystem via a projection scheme, detailed in Secs. II D 1 and II D 2. Within this subsystem, electron-electron interactions are treated beyond the static mean-field level. Conceptually, our embedding procedure can be viewed as a generalization of the band down-folding approaches commonly employed in bulk DFT+DMFT (e.g. Ref. [90]), adapted here to treat devices.

The central development of this work is the introduction of a practical finite-bias DMFT scheme that extends the equilibrium approach of Refs. [57, 59, 68] to non-equilibrium conditions, as explained in Sec. II D 3. This is achieved by employing a suitable non-equilibrium impurity solver (Sec. II D 6), which provides the many-body self-energies of the correlated subspace under bias. The self-energies are then embedded back into the full system (Sec. II D 5), enabling the calculations of observables such as the charge density, spectral functions, and in particular the steady-state current through the device (Sec. II E).

The framework is implemented in the SMEAGOL quantum transport package [30], which is interfaced with the SIESTA DFT code [91, 92].

A. System setup

A two-terminal spintronic device, such as a magnetic tunnel junction (MTJ), is modeled as infinite along the transport (z by convention) direction and divided into a central scattering region connected to semi-infinite metallic leads on the left (L) and right (R) hand side [27], as shown in Fig. 1(a). Periodic boundary conditions are applied in the transverse x-y plane, with transverse wave vector $\mathbf{k} = (k_x, k_y)$ spanning the two-dimensional Brillouin zone (BZ).

The partition into leads and the central region is implemented by using a linear combination of atomic orbitals (LCAO) basis set, in which each orbital is assigned to a specific part of the device. These basis orbitals are generally non-orthogonal. In principle, changes in the electronic structure of the central region feed back into the leads and vice versa, giving rise to interface effects. To capture these effects, a sufficient portion of each lead is included within the central region itself. As illustrated in Fig. 2(a), the formal lead/central region boundary is therefore not placed at the physical interface but rather a few layers deeper inside the leads, where the electronic structure has already relaxed to its bulk configuration.

The central region constitutes the active part of the device. In quantum transport calculations, it is typically assumed that electronic correlation effects are confined to this region, while the leads are treated within an effective single-particle description [25, 93, 94]. Thus, each lead acts as an electronic reservoir, characterized by its chemical potential, $\mu_{\rm L/R}$, and inverse temperature, $\beta_{\rm L/R}$. When both leads have identical chemical potentials and temperatures — that is, $\mu_L = \mu_R = E_{\rm F}$ and $\beta_{\rm L} = \beta_{\rm R}$ — the system is in thermodynamic equilibrium, described by the grand canonical ensemble, with $E_{\rm F}$ denoting the common Fermi energy.

The effect of a finite bias voltage, V, is modeled by shifting the chemical potentials of the leads such that $\mu_{\rm L}=E_{\rm F}+\frac{eV}{2}$ and $\mu_{\rm R}=E_{\rm F}-\frac{eV}{2}$, where e is the electron charge. Because of the metallic nature of the leads and the requirement of local charge neutrality, this shift corresponds to a rigid displacement of their entire band structures. Each lead individually remains in equilibrium, described by the Fermi-Dirac distribution functions $f_{\rm L(R)}(E,\mu_{\rm L(R)})=\left[1-e^{\beta(E-\mu_{\rm L(R)})}\right]^{-1}$, while the central region experiences an electrostatic potential drop [see Fig. 1(b)]. This drives the system out of equilibrium and produces a steady-state charge current flowing through the central region from one lead to the other.

B. NEGF formalism for the steady state transport

The quantum transport properties of a two-terminal device in the steady state are computed from the spin (σ) -, energy (E)- and k-dependent NEGF of the central region. Its retarded, advanced, and lesser/greater components are given by [95]

$$G^{\sigma r}(E, \mathbf{k}) = [(E + i0^{+})S(\mathbf{k}) - H^{\sigma}(\mathbf{k}) - \Sigma_{L}^{\sigma r}(E, \mathbf{k}) - \Sigma_{R}^{\sigma r}(E, \mathbf{k}) - \Sigma_{MB}^{\sigma r}(E, \mathbf{k})]^{-1},$$
(1)

$$G^{\sigma a}(E, \mathbf{k}) = [G^{\sigma r}(E, \mathbf{k})]^{\dagger}, \qquad (2)$$

and

$$G^{\sigma \leq}(E, \mathbf{k}) = G^{\sigma r}(E, \mathbf{k}) \left[\Sigma_L^{\sigma \leq}(E, \mathbf{k}) + \Sigma_R^{\sigma \leq}(E, \mathbf{k}) + \Sigma_R^{\sigma \leq}(E, \mathbf{k}) \right]$$

$$+ \Sigma_{\text{MB}}^{\sigma \leq}(E, \mathbf{k}) \left[G^{\sigma a}(E, \mathbf{k}), \right]$$
(3)

respectively. These satisfy the relation

$$G^{\sigma r}(E, \mathbf{k}) - G^{\sigma a}(E, \mathbf{k}) = G^{\sigma > (E, \mathbf{k}) - G^{\sigma < (E, \mathbf{k})}, (4)$$

so that only two of them are independent.

In Eq. (1), $H^{\sigma}(\mathbf{k})$ is the single-particle Hamiltonian of the central region, which also includes the electrostatic potential due to the voltage bias applied between the leads, and $S(\mathbf{k})$ is the orbital overlap. $\Sigma_{\mathrm{MB}}^{\sigma r/a}(E,\mathbf{k})$ and $\Sigma_{\mathrm{MB}}^{\sigma}(E,\mathbf{k})$ in Eq. (1) and Eq. (3) are respectively the retarded/advanced and lesser/greater many-body self-energies, which account for electron-electron

interaction. Instead, $\Sigma_{\rm L}^{\sigma\ r/a}(E, \mathbf{k})$ ($\Sigma_{\rm R}^{\sigma\ r/a}(E, \mathbf{k})$) and $\Sigma_{\rm L}^{\sigma\ \lessgtr}(E, \mathbf{k})$ ($\Sigma_{\rm R}^{\sigma\ \lessgtr}(E, \mathbf{k})$) are the retarded/advanced and lesser/greater embedding self-energies of the left-hand side (right-hand side) lead, which describe the effect of the leads on the central region. The self-energies satisfy a relation analogous to that of Eq. (4). The Hamiltonian, the orbital overlap, the Green's functions, and the self-energies are represented as square $N\times N$ matrices, where N is the number of basis orbitals within the central region. In principle, all of these matrices, except for $S(\mathbf{k})$, depend on the bias voltage, V. However, the explicit V-dependence is omitted for the sake of simplicity and will be indicated only when necessary.

Eq. (1) is the Dyson equation. The retarded and advanced Green's functions, $G^{\sigma r}(E, \mathbf{k})$ and $G^{\sigma a}(E, \mathbf{k})$, describe the energy levels in the central region, given by the spin-resolved spectral function,

$$A^{\sigma}(E, \mathbf{k}) = i[G^{\sigma r}(E, \mathbf{k}) - G^{\sigma a}(E, \mathbf{k})]. \tag{5}$$

The integral of the diagonal matrix elements of $A^{\sigma}(E, \mathbf{k})$ over the transverse wave-number, \mathbf{k} , gives the density of states (DOS).

Eq. (3) is sometimes called the Keldysh equation [96]. It describes the electron occupation of the central region. In particular, the integral of $G^{\sigma} \leq (E, \mathbf{k})$ over the energy and the wave-number gives the density matrix,

$$\rho^{\sigma} = \frac{1}{2\pi i} \frac{1}{\Omega_{\mathbf{k}}} \int_{\mathrm{BZ}} d\mathbf{k} \int_{-\infty}^{\infty} dE \ G^{\sigma} < (E, \mathbf{k}), \tag{6}$$

where $\Omega_{\mathbf{k}}$ is the volume of the transverse BZ.

The retarded embedding self-energy, $\Sigma_{\rm L(R)}^{\sigma\,r}(E,\boldsymbol{k})$, can be computed exactly using semi-analytical [97] or iterative [98] schemes. Its real part gives the energy shifts of the central-region states, while the imaginary part

$$\Gamma_{L(R)}^{\sigma}(E, \mathbf{k}) = i[\Sigma_{L(R)}^{\sigma r}(E, \mathbf{k}) - \Sigma_{L(R)}^{\sigma r}(E, \mathbf{k})^{\dagger}],$$
 (7)

describes their broadening due to coupling to the leads. The lesser/greater embedding self-energy $\Sigma_{L(R)}^{\sigma}(E, \mathbf{k})$ account for the inflow/outflow of charge from the L (R) lead to the central region. They can be obtained via the fluctuation-dissipation theorem [25],

$$\Sigma_{L(R)}^{\sigma <}(E, \mathbf{k}) = i f_{L(R)}(E, \mu_{L(R)}) \Gamma_{L(R)}^{\sigma}(E, \mathbf{k}), \qquad (8)$$

$$\Sigma_{\mathrm{L}(\mathrm{R})}^{\sigma>}(E, \mathbf{k}) = i [f_{\mathrm{L}(\mathrm{R})}(E, \mu_{\mathrm{L}(\mathrm{R})}) - 1] \Gamma_{\mathrm{L}(\mathrm{R})}^{\sigma}(E, \mathbf{k}) , \quad (9)$$

since the leads are charge reservoirs and remain in a local equilibrium. Upon the application of a bias voltage V, the embedding self-energies are rigidly shifted relative to their zero-bias values

$$\Sigma_{\mathrm{L}}^{\sigma r/a \,(\lessgtr)}(E - eV/2, \boldsymbol{k}, V) = \Sigma_{\mathrm{L}}^{\sigma r/a \,(\lessgtr)}(E, \boldsymbol{k}, V = 0) ,$$

$$\Sigma_{\mathrm{R}}^{\sigma r/a \,(\lessgtr)}(E + eV/2, \boldsymbol{k}, V) = \Sigma_{\mathrm{R}}^{\sigma r/a \,(\lessgtr)}(E, \boldsymbol{k}, V = 0) ,$$
(10)

where the explicit V-dependence has been re-introduced for clarity.

The many-body self-energy satisfies relations analogous to those in Eqs. (8) and (9) [27, 77, 99]:

$$\Sigma_{\rm MB}^{\sigma}(E, \mathbf{k}) = iF_{\rm MB}^{\sigma}(E, \mathbf{k})\Gamma_{\rm MB}^{\sigma}(E, \mathbf{k}), \tag{11}$$

$$\Sigma_{\text{MB}}^{>}(E, \mathbf{k}) = i[F_{\text{MB}}^{\sigma}(E, \mathbf{k}) - 1]\Gamma_{\text{MB}}(E, \mathbf{k}), \tag{12}$$

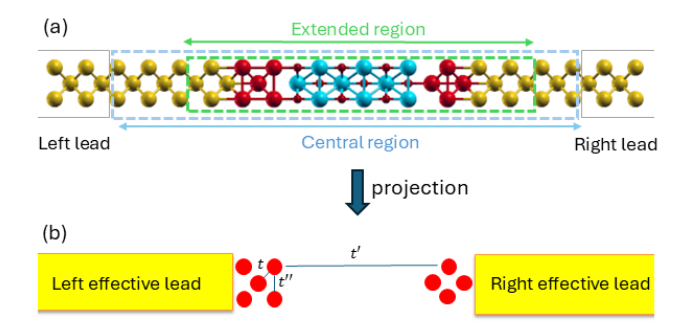
where $\Gamma^{\sigma}_{\mathrm{MB}}(E, \boldsymbol{k}) = i[\Sigma^{\sigma r}_{\mathrm{MB}}(E, \boldsymbol{k}) - \Sigma^{\sigma r}_{\mathrm{MB}}(E, \boldsymbol{k})^{\dagger}]$ describes the broadening of the spectral function due to electron-electron interaction, and $F^{\sigma}_{\mathrm{MB}}(E)$ denotes the occupation matrix of the central device region. However, unlike Eqs. (8) and (9), $F^{\sigma}_{\mathrm{MB}}(E, \boldsymbol{k})$ generally differs from the Fermi function and reduces to it only at zero bias, namely in equilibrium.

Thus, in contrast to the leads, where the fluctuationdissipation theorem provides a closed form for the retarded and lesser/greater self-energies, the many-body self-energies out of equilibrium must be calculated directly, accounting for the non-equilibrium occupation of the central region. This represents a significant challenge. In first-principles calculations, it has been addressed in a few works within the GW or three-body approximations of many-body perturbation theory, though these approaches have mostly been applied to molecular junctions [95, 100] or quasi-one-dimensional systems [101– 103]. In contrast, DFT+NEGF+DMFT studies of spintronic devices have largely been limited to zero-bias or special conditions, where the fluctuation-dissipation theorem is effectively recovered [57, 68]. This motivates the need for a general implementation valid under arbitrary non-equilibrium conditions, as presented here.

C. DFT+NEGF

DFT+NEGF neglects the retarded and lesser manybody self-energies and employs the KS Hamiltonian, $H_{\mathrm{KS}}^{\sigma}(\boldsymbol{k})$, as the single-particle Hamiltonian of the central region in Eq. (1). The embedding self-energies are likewise constructed from the corresponding KS Hamiltonians of the lead materials [104]. The exchange-correlation potential is usually treated within LSDA [12, 13] or GGA [14–16] and acts as a static mean-field interaction. For ferromagnetic metals, relevant to the spintronic devices studied in this work, this yields an effective Stoner-like description of magnetism [105]. The Green's functions in DFT+NEGF are referred to as KS Green's functions and, throughout this paper, are denoted by lowercase symbols $g^{\sigma r/a(\lessgtr)}$ to distinguish them from the manybody Green's functions introduced in Eqs. (1), (2), and (3).

The KS Hamiltonian of the central region depends functionally on the charge density ρ^{σ} , defined in Eq. (6) via the lesser Green's function. Consequently, Eqs. (1), (3), and (6) must be solved in a self-consistent manner. At finite bias, the electrostatic potential across the central region is obtained by solving the Poisson equation for the charge density at each iteration step and with the boundary conditions of Eq. (10) [30]. In certain systems, such MTJs, where the voltage drop occurs almost



The device setup used in this work. Fe/MgO/Fe junction sandwiched between simple metallic electrodes, introduced in Sec. IVB, shown as a prototypical example of a two-terminal device for DFT+NEGF calculations. Fe, Mg, and O atoms are represented by large red, cyan, and small red spheres, respectively, while the lead atoms are shown as yellow spheres. The Fe atoms define the correlated subspace. The formal lead/central region boundary is placed a few layers deeper inside the leads to ensure that interface effects are considered and that the correlated subspace does not interact directly with the leads, as required for Eq. (19) to hold. The "extended region" is indicated by the green dashed box. Atoms outside this region are not coupled to $\mathcal C$ due to the finite spatial extent of the basis orbitals. (b) The projection maps the original device onto an effective one, with renormalized hopping between correlated atoms and effective coupling to the leads.

entirely across the insulating barrier, the bias dependence can alternatively be incorporated in a non-self-consistent way by adding a linear ramp potential to the Hamiltonian. This will be the approach followed in this work, as discussed in Sec. III.

D. DMFT combined with DFT+NEGF

1. Projection onto the correlated subspace

The calculation of the many-body self-energy for all the N basis orbitals of a device's central region is practically infeasible. Often, this is also unnecessary, since in many cases electron-electron interaction beyond the static-mean field KS description is significant only for a few atoms or orbitals within the device. Therefore, we carry out a projection of the full central region onto a much smaller subspace, called the correlated subspace C, which is spanned by a limited number of orbitals. The orthogonal complement of \mathcal{C} within the central region is referred to as the "bath", \mathcal{B} , and remains described at the KS level. Then, \mathcal{B} can be further separated into two new effective leads, coupled to the correlated subspace \mathcal{C} , thereby providing a mapping from the original twoterminal device to a new, effective one, as shown in Fig. 2. DMFT will then be applied to treat this new system and the obtained self-energies will finally be backprojected to the entire one (see Sec. IID 5).

Specifically, in the ferromagnetic transition metals used in spintronic devices, the valence states consist of the 4s, 4p, and 3d orbitals. The 4s and 4p are delocalized and form broad energy bands, so that their electronic behavior is well captured by the effective single-particle KS picture. In contrast, the 3d orbitals are more localized, energetically centered around the Fermi level, and therefore, moderately correlated. As such, they are selected to span \mathcal{C} . The size of \mathcal{C} is $N_{\mathcal{C}}=2\times 5\times N_{\mathrm{TM}}$, where N_{TM} is the number of correlated transition metal atoms within our central region. The factor of 2 accounts for spin, and 5 corresponds to the number of 3d orbitals per atom. Conversely, the size of the bath is $N_{\mathcal{B}}=N-N_{\mathcal{C}}$.

The separation between \mathcal{C} and \mathcal{B} is achieved through a basis transformation that returns zero orbital overlap between \mathcal{C} and \mathcal{B} and also orthonormalizes the correlated orbitals inside \mathcal{C} , as detailed in Ref. [77]. This orthonormalization is convenient, as the impurity solvers employed in DMFT are typically formulated and implemented over an orthogonal basis set. Denoting the transformation matrix by $W(\mathbf{k})$, as defined in Eq. (10) of Ref. [77], the KS Hamiltonian and overlap matrices are transformed accordingly:

$$\bar{H}_{KS}^{\sigma}(\mathbf{k}) = \begin{pmatrix} \bar{H}_{\mathcal{C}}^{\sigma}(\mathbf{k}) & \bar{H}_{\mathcal{C},\mathcal{B}}^{\sigma}(\mathbf{k}) \\ \bar{H}_{\mathcal{B},\mathcal{C}}^{\sigma}(\mathbf{k}) & \bar{H}_{\mathcal{B}}^{\sigma}(\mathbf{k}) \end{pmatrix} =$$

$$= W(\mathbf{k})^{\dagger} H_{KS}^{\sigma}(\mathbf{k}) W(\mathbf{k}), \tag{13}$$

$$\bar{S}(\mathbf{k}) = \begin{pmatrix} 1 & 0 \\ 0 & \bar{S}_{\mathcal{B}}(\mathbf{k}) \end{pmatrix} = \\
= W(\mathbf{k})^{\dagger} S(\mathbf{k}) W(\mathbf{k}). \tag{14}$$

Here, $\bar{H}_{\mathcal{C}}^{\sigma}$ ($\bar{H}_{\mathcal{B}}^{\sigma}$) refers to the KS Hamiltonian of \mathcal{C} (\mathcal{B}), while $\bar{H}_{\mathcal{CB}}^{\sigma}(\mathbf{k})$ and $\bar{H}_{\mathcal{BC}}^{\sigma}(\mathbf{k})$ are those corresponding to the couplings between \mathcal{C} and \mathcal{B} . In contrast, the transformed overlap matrix, by construction, has the \mathcal{C} -block equal to the identity matrix, reflecting the orthonormalization of the transformed basis within \mathcal{C} , and vanishing off-diagonal blocks, because of the zero-overlap condition between \mathcal{C} and \mathcal{B} .

In second quantization, the KS Hamiltonian of \mathcal{C} reads

$$\hat{\bar{H}}_{\mathcal{C}}^{\sigma}(\mathbf{k}) = \sum_{i\lambda_i, j\lambda_j} [\bar{H}_{\mathcal{C}}^{\sigma}(\mathbf{k})]_{i\lambda_i, j\lambda_j} \hat{d}_{i\lambda_i\sigma}^{\dagger} \hat{d}_{j\lambda_j\sigma} , \qquad (15)$$

where $\hat{d}^{\dagger}_{i\lambda\sigma}$ ($\hat{d}_{i\lambda\sigma}$) is the fermionic creation (annihilation) operator for an electron with spin σ in the λ 'th orbital of the i'th atomic site. The indices i and j run over all atomic sites with correlated orbitals, while λ_i and λ_j label the correlated orbitals on the i'th and j'th atoms. For example, in a ferromagnetic transition metal with $N_{\rm TM}$ atoms having correlated 3d orbitals, we have $i,j=1,...,N_{\rm TM}$ and $\lambda_i,\lambda_j=1,...,5$. The diagonal terms in the Hamiltonian matrix, $[\bar{H}^{\sigma}_{\mathcal{C}}(\mathbf{k})]_{i\lambda_i,i\lambda_i}$, represent the orbital energies, while the off-diagonal ones, $[\bar{H}^{\sigma}_{\mathcal{C}}(\mathbf{k})]_{i\lambda_i,j\lambda'_i}$ with

 $i \neq j \ (i = j \text{ and } \lambda_i \neq \lambda_j)$, describe inter (intra)-atomic hopping integrals for atoms within C.

The Hamiltonian in Eq. (15) captures the electronic structure of \mathcal{C} within the effective single-particle KS picture of DFT+NEGF. To incorporate for electron-electron interaction, we include a multi-orbital Hubbard-like interaction term, a choice justified by the predominantly local nature of the screened Coulomb interaction in transition metals. The resulting interacting Hamiltonian for \mathcal{C} is

$$\hat{\bar{H}}_{\mathcal{C},\mathcal{U}}(\boldsymbol{k}) = \sum_{\sigma} \left[\hat{\bar{H}}_{\mathcal{C}}^{\sigma}(\boldsymbol{k}) - \hat{\bar{H}}_{\mathcal{C},dc}^{\sigma} + + \frac{1}{2} \sum_{\substack{i,\lambda_1,\lambda_2,\lambda_3,\\\lambda_4,\sigma'}} U_{\lambda_1,\lambda_2,\lambda_3,\lambda_4} \hat{d}_{i\lambda_1\sigma}^{\dagger} \hat{d}_{i\lambda_2\sigma'}^{\dagger} \hat{d}_{i\lambda_4\sigma'} \hat{d}_{i\lambda_3\sigma} \right],$$
(16)

where $U_{\lambda_1,\lambda_2,\lambda_3,\lambda_4}$ is the four-index interaction tensor. This can be parameterized in terms of the average effective Coulomb repulsion U and exchange J [106]

$$U = \frac{1}{(2l+1)^2} \sum_{\lambda_1, \lambda_2} U_{\lambda_1, \lambda_2, \lambda_1, \lambda_2}, \tag{17}$$

$$J = \frac{1}{2l(2l+1)} \sum_{\lambda_1 \neq \lambda_2} U_{\lambda_1, \lambda_2, \lambda_2, \lambda_1}.$$
 (18)

 $\bar{H}_{\mathcal{C},dc}^{\sigma}$ is the double-counting correction, which subtracts the static correlation already included at the KS mean-field level in $\hat{H}_{\mathcal{C}}^{\sigma}(\mathbf{k})$. While its exact form is unknown, several approximate schemes have been proposed for bulk systems in equilibrium [52, 54, 107, 108]. However, for open systems out of equilibrium, the proper treatment of double-counting remains an open problem, as further discussed in Sec. II D 6.

The same transformation applied to the Hamiltonian is also applied to the lead self-energy. In particular, if the system is constructed such that the leads are not directly coupled to \mathcal{C} — a condition that can be ensured by including a sufficient number of lead layers within the central region, as in Fig. 2(b) — the lead self-energy acquires the block form

$$\bar{\Sigma}_{L(R)}^{\sigma r(<)}(E, \mathbf{k}) = \begin{pmatrix} 0 & 0 \\ 0 & \bar{\Sigma}_{L(R), \mathcal{B}}^{\sigma r(<)}(\mathbf{k}) \end{pmatrix} =$$

$$= W(\mathbf{k})^{\dagger} \Sigma_{L(R)}^{\sigma r(<)}(E, \mathbf{k}) W(\mathbf{k}) . \tag{19}$$

Finally, the sum, $\Sigma_{\mathcal{B}}(\mathbf{k}) = \Sigma_{L,\mathcal{B}}(\mathbf{k}) + \Sigma_{R,\mathcal{B}}(\mathbf{k})$ describes the total coupling of the bath orbitals to the device's leads.

2. Embedding self-energies for the correlated subspace

The KS Green's function in the transformed basis acquires the same block form as the KS Hamiltonian in Eq.

(13) and it is defined as

$$\begin{pmatrix}
\bar{g}_{\mathcal{C}}^{\sigma r}(E, \mathbf{k}) & \bar{g}_{\mathcal{C}\mathcal{B}}^{\sigma r}(E, \mathbf{k}) \\
\bar{g}_{\mathcal{B}\mathcal{C}}^{\sigma r}(E, \mathbf{k}) & \bar{g}_{\mathcal{B}}^{\sigma r}(E, \mathbf{k})
\end{pmatrix} = \\
\left[E\begin{pmatrix} 1 & 0 \\ 0 & \bar{S}_{\mathcal{B}}(\mathbf{k}) \end{pmatrix} - \begin{pmatrix} \bar{H}_{\mathcal{C}}^{\sigma}(\mathbf{k}) & \bar{H}_{\mathcal{C},\mathcal{B}}^{\sigma}(\mathbf{k}) \\ \bar{H}_{\mathcal{B},\mathcal{C}}^{\sigma}(\mathbf{k}) & \bar{H}_{\mathcal{B}}^{\sigma}(\mathbf{k}) \end{pmatrix} - \begin{pmatrix} 0 & 0 \\ 0 & \bar{\Sigma}_{\mathcal{B}}(E, \mathbf{k}) \end{pmatrix}\right]^{-1}.$$
(20)

Performing the matrix inversion yields the KS Green's function of $\mathcal C$

$$\bar{g}_{\mathcal{C}}^{\sigma r}(E, \mathbf{k}) = [E - \bar{H}_{\mathcal{C}}^{\sigma}(\mathbf{k}) - \bar{H}_{\mathcal{C}, \mathcal{B}}^{\sigma}(\mathbf{k}) \bar{g}_{\mathcal{B}}^{\sigma r}(\mathbf{k}) \bar{H}_{\mathcal{B}, \mathcal{C}}^{\sigma}(\mathbf{k})]^{-1},$$
(21)

where

$$\bar{\mathfrak{g}}_{\mathcal{B}}^{\sigma r}(E, \mathbf{k}) = [E\bar{S}_{\mathcal{B}}(\mathbf{k}) - \bar{H}_{\mathcal{B}}^{\sigma}(\mathbf{k}) - \bar{\Sigma}_{\mathcal{B}}(E, \mathbf{k})]^{-1}$$
 (22)

is the retarded Green's function of the bath decoupled from $\mathcal{C}.$

Following Ref. [77], the bath can be further subdivided into $N_{\rm NI}$ basis orbitals that are coupled to \mathcal{C} , forming the so-called "extended region", and the N_{α} (N_{β}) orbitals within the central region on the left (right) of \mathcal{C} , which are not coupled to \mathcal{C} due to the finite spatial extent of the basis orbitals, as shown schematically in Fig. 2(a). Thus, the bath and \mathcal{C} -bath coupling Hamiltonians can be written in block forms as

$$\bar{H}_{\mathcal{B}}^{\sigma}(\mathbf{k}) = \begin{pmatrix} H_{\alpha\alpha}^{\sigma}(\mathbf{k}) & \bar{H}_{\alpha,\mathrm{NI}}^{\sigma}(\mathbf{k}) & H_{\alpha\beta}^{\sigma}(\mathbf{k}) \\ \bar{H}_{\alpha,\mathrm{NI}}^{\sigma}(\mathbf{k})^{\dagger} & \bar{H}_{\mathrm{NI}}^{\sigma}(\mathbf{k}) & \bar{H}_{\beta,\mathrm{NI}}^{\sigma}(\mathbf{k})^{\dagger} \\ H_{\alpha\beta}^{\sigma}(\mathbf{k})^{\dagger} & \bar{H}_{\beta,\mathrm{NI}}^{\sigma}(\mathbf{k}) & H_{\beta\beta}^{\sigma}(\mathbf{k}) \end{pmatrix} (23)$$

$$\bar{H}_{\mathcal{C}}^{\sigma}_{\mathcal{B}}(\mathbf{k}) = \begin{pmatrix} 0 & \bar{H}_{\mathcal{C}}^{\sigma}_{\mathrm{NI}}(\mathbf{k}) & 0 \end{pmatrix}, \qquad (24)$$

while the bath overlap matrix, $\bar{S}_{\mathcal{B}}(\mathbf{k})$, and the bath Green's function, $\bar{\mathfrak{g}}_{\mathcal{B}}^{\sigma r}(E,\mathbf{k})$, can be written in the same form as Eq. (23). Note that the $H_{\alpha\beta}^{\sigma}$, $H_{\alpha\alpha}^{\sigma}$, and $H_{\beta\beta}^{\sigma}$ components are written without bars [cf. Eq. (16) in Ref. [77]], as they remain unchanged under the transformation in Eq. (13).

Next, we assume that $H_{\alpha\beta}^{\sigma}(\mathbf{k}) = 0$, which implies that the N_{α} orbitals to the left of \mathcal{C} are not coupled to the N_{β} orbitals to the right, and

$$\bar{\Sigma}_{\mathcal{B}}(E, \mathbf{k}) = \begin{pmatrix} \Sigma_{\alpha\alpha}^{\sigma}(E, \mathbf{k}) & 0 & 0\\ 0 & 0 & 0\\ 0 & 0 & \Sigma_{\beta\beta}^{\sigma}(\mathbf{k}). \end{pmatrix}$$
(25)

This condition is always enforced by the user in our calculations. Consequently, Eq. (21) simplifies to

$$\bar{g}_{\mathcal{C}}^{\sigma r}(E, \mathbf{k}) = [E - \bar{H}_{\mathcal{C}}^{\sigma}(\mathbf{k}) - \bar{\Sigma}_{\mathcal{C}, NI}^{\sigma r}(E, \mathbf{k})]^{-1},$$
 (26)

where

$$\bar{\Sigma}_{\mathcal{C},\mathrm{NI}}^{\sigma,r}(E,\boldsymbol{k}) = \bar{H}_{\mathcal{C},\mathrm{NI}}^{\sigma}(\boldsymbol{k})\bar{\mathfrak{g}}_{\mathrm{NI}}^{\sigma,r}(E,\boldsymbol{k})\bar{H}_{\mathrm{NI},\mathcal{C}}^{\sigma}(\boldsymbol{k})^{\dagger}$$
(27)

is the effective retarded embedding self-energy for \mathcal{C} , with the Green's function of the NI part given by

$$\bar{\mathbf{g}}_{\mathrm{NI}}^{\sigma r}(E, \boldsymbol{k}) = \\
= \left[E \bar{S}_{\mathrm{NI}}(\boldsymbol{k}) - \bar{H}_{\mathrm{NI}}^{\sigma}(\boldsymbol{k}) - \bar{\Sigma}_{\mathrm{L,NI}}^{\sigma r}(E, \boldsymbol{k}) - \bar{\Sigma}_{\mathrm{R,NI}}^{\sigma r}(E, \boldsymbol{k}) \right]^{-1}.$$
(28)

Here, $\bar{\Sigma}_{L,NI}^{\sigma r}(E, \mathbf{k})$ and $\bar{\Sigma}_{R,NI}^{\sigma r}(E, \mathbf{k})$ are the embedding self-energies for NI from the left (α) and right (β) parts of the bath, respectively. These are defined analogously to Eqs. (62) and (63) of Ref. [77] as

$$\bar{\Sigma}_{L,NI}^{\sigma r}(E, \mathbf{k}) = \bar{K}_{NI,\alpha}^{\sigma}(E, \mathbf{k}) \mathfrak{g}_{\alpha\alpha}^{\sigma r}(E, \mathbf{k}) \bar{K}_{NI,\alpha}^{\sigma}(E, \mathbf{k})^{\dagger},
\bar{\Sigma}_{RNI}^{\sigma}(E, \mathbf{k}) = \bar{K}_{NI,\beta}^{\sigma}(E, \mathbf{k}) \mathfrak{g}_{\beta\beta}^{\sigma r}(E, \mathbf{k}) \bar{K}_{NI,\beta}^{\sigma}(E, \mathbf{k})^{\dagger},$$
(29)

where

$$\mathfrak{g}_{\alpha\alpha(\beta\beta)}^{\sigma r}(E, \mathbf{k}) = [K_{\alpha\alpha(\beta\beta)}^{\sigma}(E, \mathbf{k}) - \Sigma_{\alpha\alpha(\beta\beta)}^{\sigma}(E, \mathbf{k})]^{-1}$$
(30)

is the Green's function of the α (β) block, $\bar{K}_{\mathrm{NI},\alpha(\beta)}(E,\boldsymbol{k})=[E\bar{S}_{\mathrm{NI},\alpha(\beta)}(\boldsymbol{k})-\bar{H}^{\sigma}_{\mathrm{NI},\alpha(\beta)}(\boldsymbol{k})]$ are the corresponding coupling matrices between NI and the left (right) subsystems and $K^{\sigma}_{\alpha\alpha(\beta\beta)}(E,\boldsymbol{k})=[E\bar{S}_{\alpha\alpha(\beta\beta)}(\boldsymbol{k})-\bar{H}^{\sigma}_{\alpha\alpha(\beta\beta)}(\boldsymbol{k})]$ corresponds to the left (right) block.

By substituting $\bar{\mathfrak{g}}_{\mathrm{NI}}^{\sigma r}(E, \mathbf{k})$ from Eq. (28) into the expression for $\bar{\Sigma}_{\mathcal{C},\mathrm{NI}}^{\sigma}(E, \mathbf{k})$ in Eq. (27) and by taking the imaginary part, we obtain the broadening matrices for \mathcal{C} coupled to the new effective left and right leads

$$\bar{\gamma}_{L,C}(E, \mathbf{k}) = \bar{H}_{C,NI}(\mathbf{k}) \bar{\mathbf{g}}_{NI}^{\sigma \, r}(E, \mathbf{k}) \bar{\Gamma}_{L,NI}(E, \mathbf{k}) \times \bar{\mathbf{g}}_{NI}^{\sigma \, r}(E, \mathbf{k})^{\dagger} \bar{H}_{C,NI}(\mathbf{k})^{\dagger},$$
(31)

$$\bar{\gamma}_{R,\mathcal{C}}(E,\boldsymbol{k}) = \bar{H}_{\mathcal{C},NI}(\boldsymbol{k})\bar{\mathfrak{g}}_{NI}^{\sigma r}(E,\boldsymbol{k})^{\dagger}\bar{\Gamma}_{R,NI}(E,\boldsymbol{k})) \times \bar{\mathfrak{g}}_{NI}^{\sigma r}(E,\boldsymbol{k})\bar{H}_{\mathcal{C},NI}(\boldsymbol{k})^{\dagger},$$
(32)

as defined in Eqs. (71) and (72) of Ref. [77], with

$$\bar{\Gamma}_{L,NI}(E, \mathbf{k}) = i \left[\bar{\Sigma}_{L,NI}^{\sigma r}(E, \mathbf{k}) - \bar{\Sigma}_{L,NI}^{\sigma r}(E, \mathbf{k})^{\dagger} \right], (33)$$

$$\bar{\Gamma}_{R,NI}(E, \mathbf{k}) = i \left[\bar{\Sigma}_{R,NI}^{\sigma r}(E, \mathbf{k}) - \bar{\Sigma}_{R,NI}^{\sigma r}(E, \mathbf{k})^{\dagger} \right]. (34)$$

Finally, the lesser KS Green's function of \mathcal{C} is given by

$$\bar{g}_{\mathcal{C}}^{\sigma <}(E, \boldsymbol{k}) = \bar{g}_{\mathcal{C}}^{\sigma r}(E, \boldsymbol{k}) [\bar{\Sigma}_{L, \mathcal{C}}^{\sigma <}(E, \boldsymbol{k}) + \bar{\Sigma}_{R, \mathcal{C}}^{\sigma <}(E, \boldsymbol{k})] \bar{g}_{\mathcal{C}}^{\sigma r}(E, \boldsymbol{k})^{\dagger},$$
(35)

where the lesser embedding self-energy for the left-hand side (right-hand side) effective lead is defined, analogously to Eq. (8), as

$$\bar{\Sigma}_{L(R),\mathcal{C}}^{\sigma <}(E, \mathbf{k}) = i f_{L(R)}(E, \mu_{L(R)}) \bar{\gamma}_{L(R),\mathcal{C}}(E, \mathbf{k}). \quad (36)$$

Here, we use the chemical potential of the original electrodes. As such, while Eq. (36) is always valid in equilibrium, under non-equilibrium conditions it will hold only if the applied bias does not drop inside the portion of the device that has been incorporated into the new effective leads. This is an approximation inherent to our current implementation and should be taken into account, as it may limit its applicability. In principle, it can be easily relaxed, but doing so is involved within the present structure of the SMEAGOL code and is left for the future work. For the systems studied here the approximation, however, is well justified.

3. Non-equilibrium DMFT loop

The effective device is finally treated within DMFT. The retarded and the lesser Green's functions of \mathcal{C} are defined analogously to Eq. (1) and (3) as,

$$\bar{G}_{\mathcal{C}}^{\sigma r}(E, \mathbf{k}) = \bar{g}_{\mathcal{C}}^{\sigma r}(E, \mathbf{k}) + \bar{g}_{\mathcal{C}}^{\sigma r}(E, \mathbf{k}) \bar{\Sigma}_{\mathcal{C}}^{\sigma r}(E) \bar{G}_{\mathcal{C}}^{\sigma r}(E, \mathbf{k}), \qquad (37)$$

$$\bar{G}_{\mathcal{C}}^{\sigma} < (E, \mathbf{k}) = \bar{G}_{\mathcal{C}}^{\sigma r}(E, \mathbf{k}) [\bar{\Sigma}_{L,\mathcal{C}}^{\sigma} < (E, \mathbf{k}) + \bar{\Sigma}_{R,\mathcal{C}}^{\sigma} < (E, \mathbf{k}) + \bar{\Sigma}_{\mathcal{C}}^{\sigma} < (E)] \bar{G}_{\mathcal{C}}^{\sigma r}(E, \mathbf{k})^{\dagger}. \tag{38}$$

Here, $\bar{g}_{\mathcal{C}}^{\sigma r}(E, \mathbf{k})$ is the KS retarded Green's function defined in Eq. (26) and $\bar{\Sigma}_{L(R),\mathcal{C}}^{\sigma <}(E, \mathbf{k})$ is the lesser embedding self-energy for the left (right) effective lead in Eq. (36). $\bar{\Sigma}_{\mathcal{C}}^{\sigma r}(E)$ and $\bar{\Sigma}_{\mathcal{C}}^{\sigma <}(E)$ are the many-body retarded and the lesser self-energies, which are \mathbf{k} -independent and site diagonal due to the locality approximation of DMFT,

$$\bar{\Sigma}_{\mathcal{C}}^{\sigma\ r(<)}(E) = \begin{pmatrix} \bar{\Sigma}_{1}^{\sigma\ r(<)}(E) & 0 & \dots & 0 \\ 0 & \bar{\Sigma}_{2}^{\sigma\ r(<)}(E) & \dots & 0 \\ 0 & 0 & \dots & \bar{\Sigma}_{N_{\mathrm{TM}}}^{\sigma\ r(<)}(E) \end{pmatrix}. \tag{39}$$

Each $\bar{\Sigma}_{i}^{\sigma r(<)}(E)$ block represents the retarded (lesser) DMFT self-energy for atomic site i within the correlated subspace \mathcal{C} . The index i runs over the N_{TM} transitionmetal atoms forming the ferromagnetic layers in our spin-

tronic devices. Each block is a 5×5 matrix, corresponding to the five 3d orbitals of these atoms.

The self-energies, $\bar{\Sigma}_{\mathcal{C}}^{\sigma r}(E)$ and $\bar{\Sigma}_{\mathcal{C}}^{\sigma <}(E)$, are obtained by mapping the correlated subspace onto a set of auxiliary impurity problems, one for each atom. In analogy with DMFT for zero-bias transport [67, 68], this is achieved by enforcing the self-consistency condition that the so-called local Green's function of atom i coincides with the corresponding impurity's Green's function,

$$G_{\text{imp},i}^{\sigma r(<)}(E) = \bar{G}_{\text{loc},i}^{\sigma r(<)}(E) \equiv \frac{1}{\Omega_{\mathbf{k}}} \int d\mathbf{k} \; \bar{G}_{\mathcal{C},i}^{\sigma r(<)}(E,\mathbf{k}). \tag{40}$$

Unlike the zero-bias case, where only the retarded component must be matched, under non-equilibrium conditions, the self-consistency condition applies to both the retarded and lesser components due to the breakdown of the fluctuation-dissipation theorem (Sec. II B), except in certain special cases (Sec. II D 4).

In practice, the DMFT self-consistent cycle (schematically illustrated in Fig. 3) proceeds through the following main steps:

- i) Compute the many-body retarded and the lesser Green's functions of the correlated subsystem in Eqs. (37) and (38). For the first iteration, the many-body self-energies $\bar{\Sigma}_{\mathcal{C}}^{\sigma r}(E)$ and $\bar{\Sigma}_{\mathcal{C}}^{\sigma <}(E)$ are generally assumed to vanish.
- ii) For each atom i, extract the corresponding diagonal block $\bar{G}_{\mathcal{C},i}^{\sigma r(<)}(E,\mathbf{k})$ from $\bar{G}_{\mathcal{C}}^{\sigma r(<)}(E,\mathbf{k})$, and compute the local retarded (lesser) Green's function.
- iii) Construct the retarded and lesser dynamical mean fields for each atom

$$\bar{\mathcal{G}}_{\mathrm{DF},i}^{\sigma r}(E) = \left[\bar{G}_{\mathrm{loc},i}^{\sigma r}(E)^{-1} + \bar{\Sigma}_{i}^{\sigma r}(E)\right]^{-1}, \quad (41)$$

$$\bar{\mathcal{G}}_{\mathrm{DF},i}^{\sigma <}(E) = \bar{\mathcal{G}}_{\mathrm{DF},i}^{\sigma r}(E)\Delta_{i}^{<}(E)\bar{\mathcal{G}}_{\mathrm{DF},i}^{\sigma r}(E)^{\dagger}, \tag{42}$$

where

$$\Delta_{i}^{\leq}(E) = \left[\bar{G}_{\text{loc},i}^{\sigma r}(E)\right]^{-1} \bar{G}_{\text{loc},i}^{\sigma \leq}(E) \left[\bar{G}_{\text{loc},i}^{\sigma r}(E)^{\dagger}\right]^{-1} - \bar{\Sigma}_{i}^{\sigma \leq}(E).$$

$$(43)$$

is the lesser hybridization function.

iv) Define the non-interacting impurity's retarded and lesser Green's functions as

$$g_{\text{imp},i}^{\sigma r}(E) \equiv \bar{\mathcal{G}}_{\text{DF},i}^{\sigma r}(E), \quad g_{\text{imp},i}^{\sigma <}(E) \equiv \bar{\mathcal{G}}_{\text{DF},i}^{\sigma <}(E).$$
 (44)

v) Solve each impurity problem using an appropriate non-equilibrium impurity solver. The specific solver employed in our work is detailed in Sec. II D 6. For each impurity, the solver yields the impurity's retarded and lesser many-body self-energies, denoted by $\Sigma_{\text{imp},i}^{\sigma r}(E)$ and $\Sigma_{\text{imp},i}^{\sigma <}(E)$, respectively, and the corresponding impurity's Green's functions,

$$G_{\text{imp},i}^{\sigma r}(E) = \left[g_{\text{imp},i}^{\sigma r}(E)^{-1} - \Sigma_{\text{imp},i}^{\sigma r}(E)\right]^{-1}, \tag{45}$$

$$G_{\text{imp},i}^{\sigma <}(E) = G_{\text{imp},i}^{\sigma r}(E) \left[\Delta_{i}^{<}(E) + \Sigma_{\text{imp},i}^{\sigma <}(E)\right] G_{\text{imp},i}^{\sigma r}(E)^{\dagger}. \tag{46}$$

vi) Update the DMFT retarded and lesser self-energies by setting $\bar{\Sigma}_{i}^{\sigma r}(E) = \Sigma_{\mathrm{imp},i}^{\sigma r}(E)$ and $\bar{\Sigma}_{i}^{\sigma}(E) = \Sigma_{\mathrm{imp},i}^{\sigma}(E)$ in Eq. (39). Return to step (i) and iterate until the self-consistency condition in Eq. (40) is satisfied.

4. Rigid shift approximation

In certain situations, the full non-equilibrium DMFT procedure described above can be simplified. In particular, when the correlated atoms are strongly coupled to one lead and are separated from the opposite lead by a sufficiently thick barrier — so that their interaction with that well-separated lead is negligible — they can be considered to be in equilibrium with the lead they are coupled to. In this limit, the fluctuation-dissipation theorem is effectively recovered.

This allows us to apply the "rigid shift approximation", introduced in Ref. [59]. Each block of the retarded and lesser correlated subspace's self-energies in Eq. (39) can be obtained through relations similar to Eq. (10) and Eq. (8), namely

$$\bar{\Sigma}_i^{\sigma r}(E \pm eV/2, V) = \bar{\Sigma}_i^{\sigma r}(E, V = 0), \qquad (47)$$

$$\bar{\Sigma}_{i}^{\sigma} < (E, V) = i f_{L(R)}(E, \mu_{L(R)}) \bar{\Gamma}_{i}^{\sigma}(E, V) , \qquad (48)$$

where $\bar{\Gamma}_i^{\sigma}(E,V)=i[\tilde{\Sigma}_i^{\sigma}{}^r(E,V)-\bar{\Sigma}_i^{\sigma}{}^r(E,V)^{\dagger}]$. The minus (plus) sign in Eq. (47) and the Fermi function $f_{\rm L(R)}$ in Eq. (48) are used when the atom i is coupled to the left-hand side (right-hand side) lead. By using this approach, only the retarded self-energy $\bar{\Sigma}_i^{\sigma}{}^r(E,V=0)$ at zero-bias needs to be computed; the lesser and retarded components at finite bias can then be obtained directly, thus greatly reducing the computational effort.

In practice, however, we find that a straightforward application of the rigid-shift approximation often leads to poor current conservation, as it neglects the change in hybridization between the leads and the correlated orbitals induced by the electrostatic potential drop. To address this shortfall, we compute $\Sigma_i^{\sigma r}(E,V)$ using an equilibrium calculation with this electrostatic potential added to the zero-bias Kohn-Sham Hamiltonian of the central region, and then obtain the corresponding lesser DMFT self-energy via Eq. (48).

5. Back-projection to the CR

Once the DMFT self-energy of $\mathcal C$ has been calculated, we can straightforwardly construct the self-energy of the full central region as

$$\bar{\Sigma}_{\mathrm{MB}}^{\sigma \ r(<)}(E) = \begin{pmatrix} \bar{\Sigma}_{\mathrm{MB},\mathcal{C}}^{\sigma \ r(<)}(E) & 0\\ 0 & 0 \end{pmatrix}, \tag{49}$$

and apply the inverse transformation of Eq. (13) to express the many-body self-energy in the original basis,

$$\Sigma_{\rm MB}^{\sigma \ r(<)}(E, \mathbf{k}) = W(\mathbf{k})^{-1} \, \bar{\Sigma}_{\rm MB}^{\sigma \ r(<)}(E) \, W(\mathbf{k})^{-1}. \quad (50)$$

Then, $\Sigma_{\text{MB}}^{\sigma r(<)}(E, \mathbf{k})$ can then be used to compute the Green's functions defined in Eqs. (1) and (3), and thereby the spectral function [Eq. (5)], the density matrix [Eq. (6)], and the charge current defined in Sec. II E.

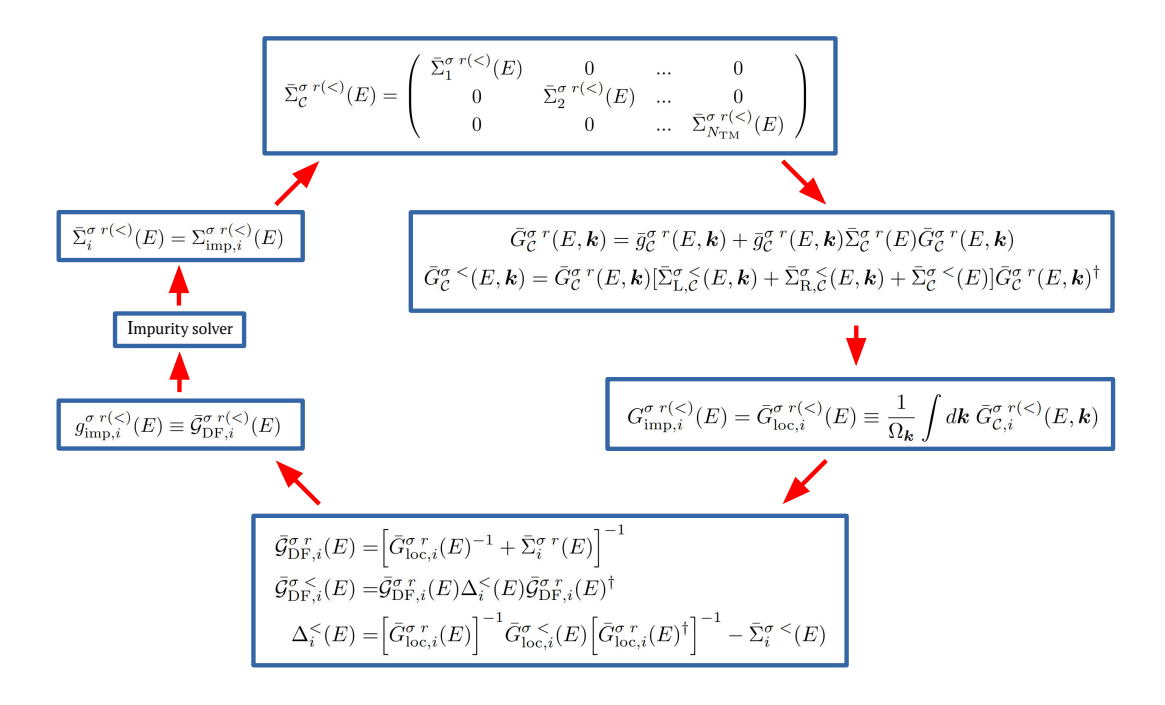


FIG. 3. Schematic representation of the DMFT loop

6. Impurity solver

At equilibrium, the impurity problem is often solved with high accuracy — up to stochastic noise — using continuous-time quantum Monte Carlo (CTQMC) methods [109], formulated on the imaginary frequency axis. To obtain real-frequency observables such as spectral functions, these results must be analytically continued to the real axis, a numerically ill-posed procedure [110]. Extending CTQMC methods to non-equilibrium systems is significantly more challenging, as it requires real-time simulations along the Keldysh contour [111-115], a task that suffers from severe sign problems and an exponential growth in computational cost with simulation time. Although recent advances, such as the steadystate inchworm CTQMC algorithm [88], have reduced the computational cost by several orders of magnitude and enabled the calculation of frequency-dependent steadystate quantities, applications have so far been limited to the single-orbital Anderson impurity model. Unfortunately, they remain computationally prohibitive for realistic multi-orbital impurity problems.

Given our focus on transition metals, which present moderate correlations, we adopt a more computationally efficient impurity solver based on second-order perturbation theory in the electron-electron interaction [25, 57, 116]. This approach can be formulated directly on the real energy axis and has been shown in previous studies to produce results in good agreement with experimental photoemission spectrum of transition metals thin films [57, 117].

In our calculations, we assume that both the retarded

and lesser components of the impurity Green's function, as well as the self-energy, are diagonal in orbital space. This significantly reduces the computational cost. For the systems considered here, this assumption is well justified due to their cubic symmetry and is routinely utilized in the literature [52, 118]. In less symmetric systems, however, the diagonal approximation may not hold, and neglecting orbital off-diagonal elements introduces an approximation whose significance must be assessed on a case-by-case basis.

The retarded component of the impurity self-energy contains both first- and second-order terms in the Coulomb interaction,

$$\Sigma_{\text{imp},i\lambda}^{\sigma r}(E) \approx \Sigma_{\text{imp},i\lambda}^{\sigma r(1)} + \Sigma_{\text{imp},i\lambda}^{\sigma r(2)}(E), \tag{51}$$

while the lesser component only contains second-order terms,

$$\Sigma_{\mathrm{imp},i\lambda}^{\sigma <}(E) \approx \Sigma_{\mathrm{imp},i\lambda}^{\sigma < (2)}(E).$$
 (52)

The subscript λ denotes the orbital of the impurity i, as in Eq. (16).

The first order contribution to the retarded self-energy takes the well-known Hartree-Fock form:

$$\Sigma_{\mathrm{imp},i\lambda}^{\sigma\ r(1)}(E) = \sum_{i\lambda_{1}\sigma_{1}} U_{i\lambda i\lambda_{1}i\lambda i\lambda_{1}}^{\sigma\sigma_{1}\sigma\sigma_{1}} n_{i\lambda_{1}}^{\sigma_{1}} - \sum_{i\lambda_{1}} U_{i\lambda i\lambda_{1}i\lambda_{1}i\lambda_{1}i\lambda}^{\sigma\sigma\sigma\sigma} n_{i\lambda_{1}}^{\sigma},$$

$$(53)$$

which is local in time and therefore energy-independent. Here, $n_{i\lambda}^{\sigma}=-\mathrm{i}\int\frac{dE}{2\pi}g_{\mathrm{imp}}^{\sigma<}i\lambda(E)$ denotes the occupation of orbital λ with spin σ on impurity i, where $g_{\mathrm{imp},i\lambda}^{\sigma<}(E)$ is

the corresponding impurity Green's function defined in Eq. (44).

The second-order contributions to the retarded and lesser self-energies are given by

$$\operatorname{Im}\left[\Sigma_{\mathrm{imp},i\lambda}^{\sigma\,r(2)}(E)\right] = -\pi \sum_{i\lambda_{1}i\lambda_{2}i\lambda_{3}\sigma_{1}} U_{i\lambda_{i}\lambda_{1}i\lambda_{2}i\lambda_{3}}^{\sigma\sigma_{1}\sigma\sigma_{1}} U_{i\lambda_{3}i\lambda_{2}i\lambda_{1}i\lambda}^{\sigma\sigma_{1}\sigma\sigma_{1}\sigma_{1}} \int d\varepsilon_{1}d\varepsilon_{2}\rho_{i\lambda_{1}\sigma_{1}}(\varepsilon_{1})\rho_{i\lambda_{2}\sigma}(\varepsilon_{2})\rho_{i\lambda_{3}\sigma_{1}}(\varepsilon_{1} + \varepsilon_{2} - E) \times (54)$$

$$\{\tilde{f}_{i\lambda_{1}\sigma_{1}}(\varepsilon_{1})\tilde{f}_{i\lambda_{2}\sigma}(\varepsilon_{2}) + \left[1 - \tilde{f}_{i\lambda_{1}\sigma_{1}}(\varepsilon_{1}) - \tilde{f}_{i\lambda_{2}\sigma}(\varepsilon_{2})\right]\tilde{f}_{i\lambda_{3}\sigma_{1}}(\varepsilon_{1} + \varepsilon_{2} - E)\}$$

$$+\pi \sum_{i\lambda_{1}i\lambda_{2}i\lambda_{3}} U_{i\lambda_{3}i\lambda_{1}i\lambda_{2}i\lambda_{3}}^{\sigma\sigma\sigma\sigma} U_{i\lambda_{3}i\lambda_{1}i\lambda} \int d\varepsilon_{1}d\varepsilon_{2}\rho_{i\lambda_{1}\sigma}(\varepsilon_{1} + \varepsilon_{2} - E)\rho_{i\lambda_{2}\sigma}(\varepsilon_{2})\rho_{i\lambda_{3}\sigma}(\varepsilon_{1}) \times$$

$$\{\tilde{f}_{i\lambda_{2}\sigma}(\varepsilon_{2})\tilde{f}_{i\lambda_{3}\sigma}(\varepsilon_{1}) + \left[1 - \tilde{f}_{i\lambda_{2}\sigma}(\varepsilon_{2}) - \tilde{f}_{i\lambda_{3}\sigma}(\varepsilon_{1})\right]\tilde{f}_{i\lambda_{1}\sigma}(\varepsilon_{1} + \varepsilon_{2} - E)\}$$

$$\Sigma_{\mathrm{imp},i\lambda}^{\sigma<(2)}(E) = 2\pi i \sum_{i\lambda_{1}i\lambda_{2}i\lambda_{3}\sigma_{1}} U_{i\lambda_{i}\lambda_{1}i\lambda_{2}i\lambda_{3}}^{\sigma\sigma\sigma\sigma} U_{i\lambda_{3}i\lambda_{2}i\lambda_{1}i\lambda} \int d\varepsilon_{1}d\varepsilon_{2}\rho_{i\lambda_{1}\sigma_{1}}(\varepsilon_{1})\rho_{i\lambda_{2}\sigma}(\varepsilon_{2})\rho_{i\lambda_{3}\sigma_{1}}(\varepsilon_{1} + \varepsilon_{2} - E) \times (55)$$

$$\tilde{f}_{i\lambda_{1}\sigma_{1}}(\varepsilon_{1})\tilde{f}_{i\lambda_{2}\sigma}(\varepsilon_{2}) \left[1 - \tilde{f}_{i\lambda_{3}\sigma_{1}}(\varepsilon_{1} + \varepsilon_{2} - E)\right]$$

$$-2\pi i \sum_{i\lambda_{1}i\lambda_{2}i\lambda_{3}} U_{i\lambda_{i}\lambda_{1}i\lambda_{2}i\lambda_{3}}^{\sigma\sigma\sigma\sigma} U_{i\lambda_{i}\lambda_{1}i\lambda_{2}i\lambda_{3}i\lambda_{1}i\lambda} \int d\varepsilon_{1}d\varepsilon_{2}\rho_{i\lambda_{1}\sigma}(\varepsilon_{1} + \varepsilon_{2} - E)\rho_{i\lambda_{2}\sigma}(\varepsilon_{2})\rho_{i\lambda_{3}\sigma}(\varepsilon_{1}) \times$$

$$\tilde{f}_{i\lambda_{2}\sigma}(\varepsilon_{2})\tilde{f}_{i\lambda_{3}\sigma}(\varepsilon_{1}) \left[1 - \tilde{f}_{i\lambda_{1}\sigma}(\varepsilon_{1} + \varepsilon_{2} - E)\right],$$

while the real part of the retarded self-energy is obtained from the Kramers-Kronig relations. Here, $\rho_{i\lambda\sigma}(E) = -\frac{1}{\pi}\mathrm{Im}g^{\sigma\,r}_{\mathrm{imp},i\lambda}(E)$ denotes the spectral function of orbital λ with spin σ on impurity i, and $\tilde{f}_{i\lambda\sigma}(E)$ is the corresponding generalized Fermi function defined as

$$\tilde{f}_{i\lambda\sigma}(E) = \frac{g_{\text{imp},i\lambda}^{\sigma<}(E)}{2\pi\rho_{i\lambda\sigma}(E)}.$$
(56)

The numerical integrations (convolutions) are performed using the uniform mesh and the trapezoid rule integration.

The first-order term corresponds to an on-site energy shift that adds to the double-counting correction in Eq. (16). In previous implementations [57], limited to zero bias, the sum of these terms was approximated by the effective U potential of the DFT+U formulation by Dudarev et al. [119]. In the present work, since the proper treatment of double-counting corrections in transport calculations at finite bias remains an open problem and the first-order term is numerically difficult to con-

verge, we assume that these contributions cancel exactly and therefore we neglect both.

The U potential and the second-order self-energy generally have opposite effects in transition-metal ferromagnets: the former enhances the spin-splitting already overestimated by DFT, while the latter tends to reduce it. Accordingly, in this work the omission of the U potential is compensated by adopting smaller effective U and J values in the evaluation of $\Sigma_{\mathrm{imp},i\lambda}^{\sigma\,r(2)}(E)$. At zero bias, this approximation yields results consistent with Refs. [59, 68] for Fe/MgO and Co/Cu junctions, where the first-order term was explicitly included, indicating that both approaches are equivalent for our practical purposes.

E. Charge current

The expression for the charge current flowing from the non-interacting left-hand side (right-hand side) lead into the CR of a two-terminal device in steady-state conditions was derived by Meir and Wingreen in their seminal paper [94], and is given by

$$I_{L(R)} = \frac{ie}{h} \frac{1}{\Omega_{\mathbf{k}}} \sum_{\sigma} \int d\mathbf{k} \int_{-\infty}^{\infty} dE \operatorname{Tr} \Big[f_{L(R)}(E, \mu_{L(R)}) \Gamma_{L(R)}^{\sigma}(E, \mathbf{k}) A^{\sigma}(E, \mathbf{k}) + i \Gamma_{L(R)}^{\sigma}(E, \mathbf{k}) G^{\sigma} (E, \mathbf{k}) \Big],$$
 (57)

where $G^{\sigma}(E, \mathbf{k})$, $A^{\sigma}(E, \mathbf{k})$, and $\Gamma_{L(R)}^{\sigma}(E, \mathbf{k})$ are defined in Eqs. (3), (5), and (7), respectively. Although Eq. (57) was originally derived assuming an orthonormal basis, it remains valid for the non-orthogonal case as

well [120][121].

Since charge conservation implies that $I_{\rm L} = -I_{\rm R}$, the current through the CR is usually expressed in the symmetrized form, $I = (I_{\rm L} - I_{\rm R})/2$, a convention adopted

here. In practice, however, some care is required in the calculations. Although DMFT is a conserving many-body theory in the Baym-Kadanoff sense [54], ensuring charge conservation in practice can be challenging due to the employed approximations (e.g., in the implementation of the impurity solvers) and numerical error propagation. Thus, we explicitly verify current conservation in all our calculations, as detailed in Sec. A1, finding generally satisfactory results.

The current can then be expressed as the sum of two contributions, which we refer to as the coherent and incoherent parts,

$$I^{\sigma} = I_{\rm C}^{\sigma} + I_{\rm IC}^{\sigma}. \tag{58}$$

This decomposition follows from Eq. (4), together with the expressions for the lesser and greater components of the lead and many-body self-energies given in Eqs. (8) and (11). The coherent contribution reads

$$I_{\rm C}^{\sigma} = \frac{e}{h} \int_{-\infty}^{\infty} dE \, T^{\sigma}(E) \big[f_{\rm L}(E) - f_{\rm R}(E) \big], \qquad (59)$$

where $T^{\sigma}(E)$ denotes the transmission coefficient, given by

$$T^{\sigma}(E) = \frac{1}{\Omega_{\mathbf{k}}} \int_{BZ} d\mathbf{k} \operatorname{Tr} \left[\Gamma_{L}^{\sigma}(E, \mathbf{k}) G^{\sigma r}(E, \mathbf{k}) \times \Gamma_{R}^{\sigma}(E, \mathbf{k}) G^{\sigma r}(E, \mathbf{k})^{\dagger} \right].$$

$$(60)$$

Equation (59) is the generalization of the Laudauer-Büttiker formula to finite bias (see, for example, reference [20, 26, 30]). The incoherent contribution, instead, is

$$I_{\rm IC}^{\sigma} = \frac{e}{2h \Omega_{\mathbf{k}}} \int_{\rm BZ} d\mathbf{k} \int dE \operatorname{Tr} \Big\{ \big[f_{\rm L}(E) - F_{\rm MB}^{\sigma}(E, \mathbf{k}) \big] \Gamma_{\rm MB}^{\sigma}(E) \\ \times G^{\sigma r}(E, \mathbf{k})^{\dagger} \Gamma_{\rm L}^{\sigma}(E, \mathbf{k}) G^{\sigma r}(E, \mathbf{k}) \Big\} \\ - \operatorname{Tr} \Big\{ \big[f_{\rm R}(E) - F_{\rm MB}^{\sigma}(E, \mathbf{k}) \big] \Gamma_{\rm MB}^{\sigma}(E) G^{\sigma r}(E, \mathbf{k})^{\dagger} \\ \times \Gamma_{\rm R}^{\sigma}(E, \mathbf{k}) G^{\sigma r}(E, \mathbf{k}) \Big\}.$$

$$(61)$$

In DFT+NEGF, there is no many-body self-energy, and thus the incoherent contribution vanishes. The current is therefore solely given by Eq. (59), with $T^{\sigma}(E)$ evaluated using the KS Green's function, $g^{\sigma r}(E, \mathbf{k})$. Accordingly, charge transport is described as the coherent transmission of electrons through the central region and is determined by the occupation of the incoming and out-coming states, $f_{\rm L}$ and $f_{\rm R}$. The integrand in Eq. (59) is significantly different from zero only within an energy range approximately spanning from $E_{\rm F} - eV/2$ to $E_{\rm F} + eV/2$, referred to as the bias window. Thus, in practice, the current is often approximated by integrating T(E) over this window.

Within DFT+NEGF+DMFT, both the coherent and incoherent contributions to the current may become significant. The coherent part, $I_{\rm C}$, still corresponds to the

current arising from transmission through the central region, but is now evaluated using the many-body retarded Green's function, and therefore reflects a modified electronic structure compared to the DFT KS one. Importantly, due to the imaginary part of the many-body self-energy, the electronic states are not only shifted in energy but also acquire a finite lifetime. This already partially breaks the notion of perfectly coherent transport, despite the conventional terminology. A similar effect has been reported within the Kubo formalism under the "bare-bubble" approximation implemented with DMFT Green's functions [122]. In our calculations based on Eq. (59), this finite lifetime generally leads to a reduction of the transmission coefficient [31, 68], and consequently, of the current.

In contrast, the properly defined incoherent contribution to the current captures the impact of inelastic scattering on transport. Notably, Eq. (61) resembles Eq. (59), but with the out-of-equilibrium electron distribution of the central region, F_{MB}^{σ} , and the many-body broadening matrix, $\Gamma_{\mathrm{MB}}^{\sigma}$, replacing f_{R} (f_{L}) and $\Gamma_{\mathrm{R}}^{\sigma}$ ($\Gamma_{\mathrm{L}}^{\sigma}$) in the first (second) term of the integrand. This suggests an intuitive picture in which the effect of electron-electron interactions can be represented by an additional "virtual electrode", characterized by the many-body self-energy and an effective distribution function $F_{\rm MB}(E, \mathbf{k})$. Then, $I_{\rm IC}$ can be interpreted as the current flowing from the left-hand side lead into this virtual electrode and subsequently from there into the right-hand side lead. Crucially, once electrons enter the virtual electrode, they may re-emerge with modified energy and phase, thereby mimicking inelastic scattering events arising from electron-electron interaction. This picture provides a natural analogy to the de-phasing Büttiker probe concept [47], wherein phase-breaking and energy-dissipating processes are captured through a fictitious, current-conserving voltage probe [123]. In contrast, DMFT provides a quantitative, atomistic, and theoretically grounded framework to address this behavior.

The incoherent contribution to the current has often been neglected in literature. However, in some systems, it can have a significant impact, leading to a substantial increase in the total current with bias [59]. In this work, we generally compute the total current using the original Meir-Wingreen formula and estimate $I_{\rm IC}$ by subtracting $I_{\rm C}$ from it, rather than applying Eq. (61), which is more complex to implement.

III. COMPUTATIONAL DETAILS

The DFT+NEGF calculations are performed using the LSDA [12, 13] for the exchange-correlation functional. The leads' self-energies are calculated using the semi-analytic algorithm from Ref. [97]. Norm-conserving Troullier-Martins pseudopotentials [124] are employed to treat the core electrons. Valence states are expanded using a numerical atomic orbital basis set, which includes

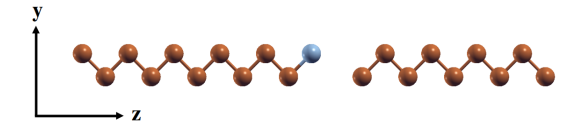


FIG. 4. The Cu/Co device investigated in this work. A Co layer is attached to a left Cu lead and separated from a right Cu lead by a 4 Å vacuum gap. Periodic boundary conditions are applied in the plane transverse to the stack.

multiple- ζ and polarized functions [91]. The electronic temperature is set to 300 K, and the real space mesh is determined by an equivalent energy cutoff of 400 Ry.

At zero-bias, the DFT density matrix, given by Eq. (6), is computed self consistently using a 20×20 transverse k-point mesh. The integration over the energy is performed using a semi-circular contour in the complex energy plane [30]. In this approach, 16 poles are used to represent the Fermi distribution, while 16 energy points are sampled along both the semi-circular arc and the imaginary line that forms the contour. The converged density matrix is read as an input for a non-self-consistent DFT calculation using a 200×200 transverse k-mesh to obtain the zero-bias DFT DOS and transmission coefficient. This is enough for resolving the transmission function over the transverse BZ in the case of tunneling. All energy values are shifted to align the Fermi level at 0 eV.

Finite-bias calculations are performed non-self-consistently, using the Hamiltonian of the central region calculated at zero-bias with an additional ramp potential [125] that reproduces the linear voltage drop across the MgO insulating barrier (vacuum gap) in Fe/MgO/Fe MTJ (Cu/Co/vacuum/Co), namely $V_e(z) = -eVz/l + eV/2$ where z = 0 (z = l) corresponds to the beginning (end) of the barrier (gap), as in Fig. 1. Similar to the equilibrium case, a 200×200 transverse k-mesh is used to obtain the finite bias DFT DOS and transmission coefficient.

DMFT calculations are performed assuming general orbital-dependent screened Coulomb interaction parameters for the 3d orbitals of Co and Fe. These parameters are expressed in terms of Slater integrals F^0 , F^2 and F^4 (see reference [126]). The ratio F^4/F^2 is assumed to correspond to the atomic value ≈ 0.625 (Ref. [127]). The average U and J interaction parameters are given through the relations $U = F^0$ and $J = (F^2 + F^4)/14$.

The local Green's function in the DMFT loop [68] is calculated by summing the retarded Green's function over 20×20 k points, whereas a 50×50 k-mesh is considered to plot the DMFT DOS and transmission coefficient. The second-order contribution to the self-energy in the impurity solver is computed on an energy grid comprising 4000 (6000) points and extending from -10 eV to 10 eV (-25 eV to 15 eV) at low bias for the Cu/Co/vacuum/Cu system (Fe/MgO/Fe MTJ).

IV. RESULTS

A. Cu/Co/vacuum/Cu

The first system investigated comprises a Co monolayer attached to a left-hand side Cu lead and separated from a right-hand side Cu lead by a 4 Å-long vacuum gap, as shown in Fig. 4(a). At finite bias, the potential drops within this gap. The setup mimics STM studies of magnetic surfaces. While a fully quantitative STM simulation would require the use of a large supercell with the right lead attached to a tip [77] –whose geometry and electronic structure may be nontrivial (e.g., [125, 128]) – the essential non-equilibrium physics related to the potential drop and charge current flowing through the central region is expected to be well captured already by our simplified system. The correlated subspace, \mathcal{C} is spanned only by the Co 3d orbitals, whereas the Cu 3d orbitals are fully occupied and therefore play a negligible role over the correlation effects. We employ an average on-site Coulomb and exchange interaction parameters of U = 1.5 eV and J = 0.5 eV, respectively.

1. Zero-bias electronic structure

The 3d-Co PDOS calculated with DFT and DMFT at zero-bias are shown in Fig. 5(a), illustrating the effect of static versus dynamical correlations. The DFT result (blue curve) exhibits a pronounced spin-splitting: the spin-up states (majority states) are almost entirely occupied, with a main peak at approximately -1.3 eV, whereas the spin-down states (minority states) extend from low energies across $E_{\rm F}$ up to about 0.7 eV. DMFT leads to a redistribution of the PDOS (red curve), resulting in a reduced spin-splitting — qualitatively similar to what has been reported in many DMFT studies of transition metal ferromagnets [55–57, 59, 68, 117]. This is the effect introduced by the real part of the retarded DMFT self-energy, shown in Fig. 6 (averaged over all five 3d orbitals). In the spin-up channel, $\text{Re}[\Sigma_{\text{avg}}^{r\uparrow}(E)]$ is large and positive, pushing the PDOS upward in energy toward $E_{\rm F}$. Conversely, in the spin-down channel, $\operatorname{Re}[\Sigma_{\operatorname{avg}}^{r\downarrow}(E)]$ becomes negative at ~ 0.2 eV, shifting the high-energy part of the PDOS downward toward $E_{\rm F}$ and thereby sharpening its main peak.

The imaginary part of the retarded DMFT self-energy vanishes at $E_{\rm F}$ and exhibits the typical behavior for a Fermi liquid, namely ${\rm Im}[\Sigma_{\rm avg}^{r\,\sigma}(E)] \propto -(E-E_{\rm F})^2$ at low energies. Furthermore, it is related to the lesser DMFT self-energy via the fluctuation-dissipation relation in Eq. (11), reflecting the occupation of electronic states according to the Fermi-Dirac distribution in equilibrium.

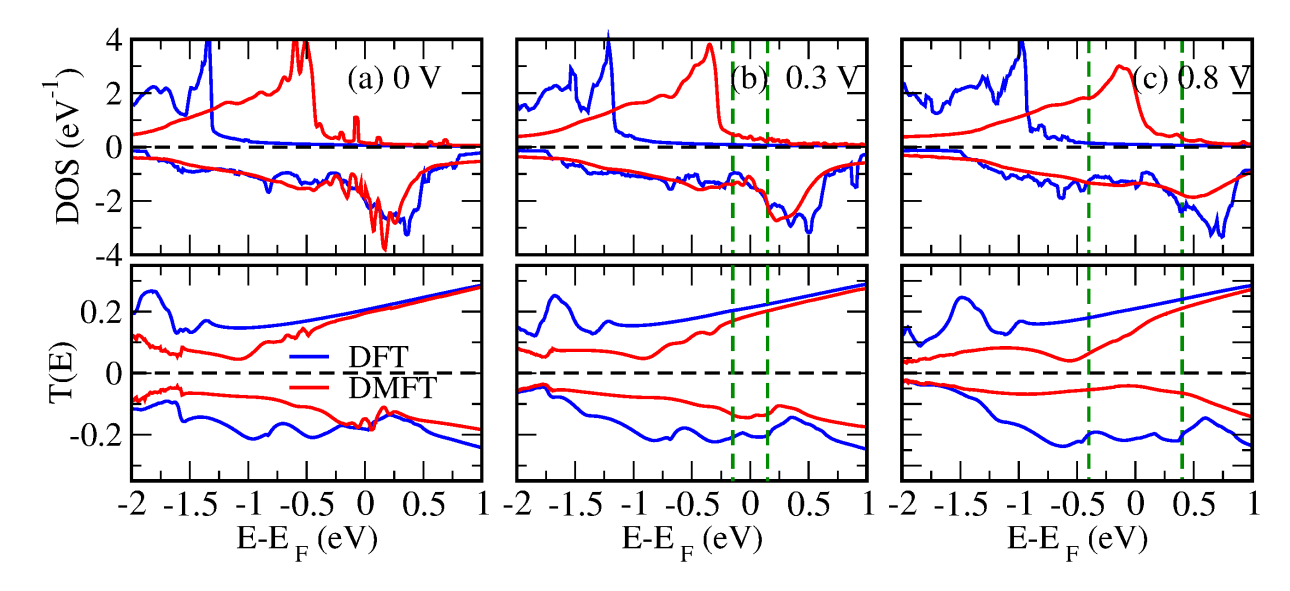


FIG. 5. DFT and DMFT 3d-Co PDOS and transmission coefficient at (a) V = 0 V, (b) V = 0.3 V, and (c) V = 0.8 V. Spin-up (down) values are shown positive (negative).

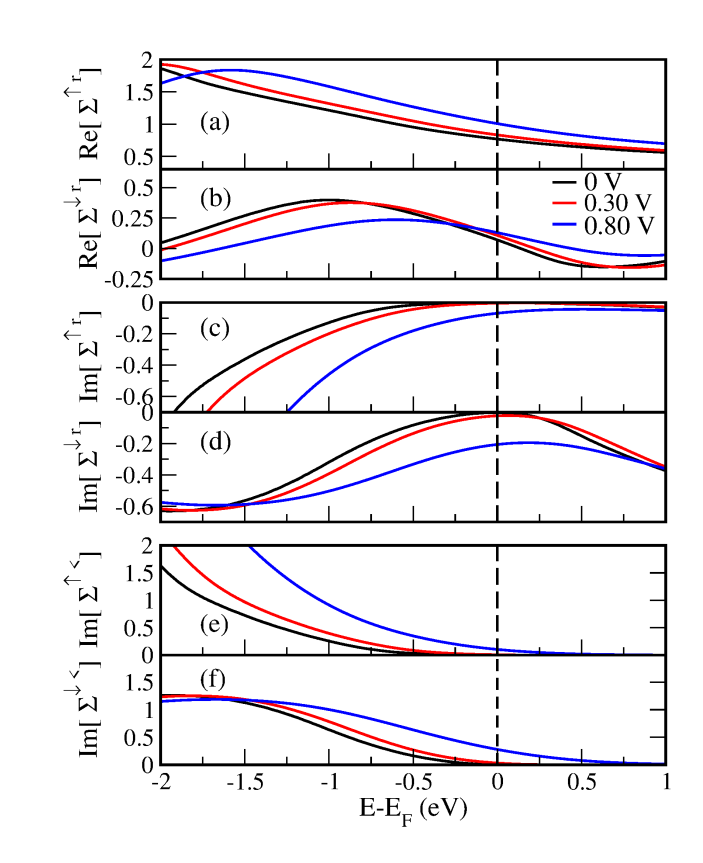


FIG. 6. DMFT self-energy for Co, averaged over all the 3d orbitals, at V=0 V, V=0.3 V, and V=0.8 V. Top panel: real part of the retarded component. Middle panel: imaginary part of the retarded component. Bottom panel: lesser component.

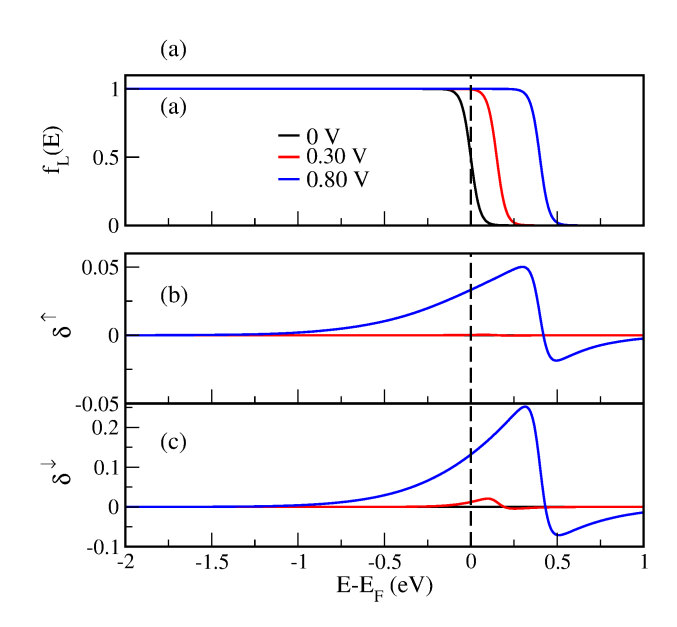


FIG. 7. (a) Fermi function of the Cu left lead attached to the Co layer. In panel (b) and (c) we show the difference $\delta^{\sigma} = f(E, \mu_{\rm L}) - F^{\sigma}_{\rm MB}(E)$, averaged over all 3d orbitals, at V=0 V, 0.3 V, and 0.75 V.

2. Finite-bias electronic structure

Upon the application of a finite bias voltage V, the 3d-Co PDOS shifts upward almost rigidly by eV/2, reflecting the strong coupling of the Co layer to the left lead. This effect is clearly visible in both the DFT and DMFT results shown in Figs. 5(b) for V=0.3 V and 5(c) for 0.8 V. However, besides this somewhat trivial shift, the most interesting finding is that the imaginary part of the DMFT self-energy deviates from the Fermi-liquid

behavior. Specifically, $\operatorname{Im}[\Sigma_{\operatorname{avg}}^{r,\uparrow}(E_{\operatorname{F}})]$ becomes finite and increases with bias (Fig. 6), indicating a loss of coherence due to electronic excitations. This displays in the progressive broadening and smoothing of the DMFT PDOS [Fig. 5(b) and (c)], particularly in the spin-down channel — an effect that is, of course, absent in the effective single-particle DFT picture.

The departure from the Fermi-liquid regime at finite bias is also evident in the breakdown of the fluctuationdissipation theorem. Specifically, the lesser DMFT selfenergy $\Sigma_{\text{avg}}^{<\sigma}(E)$, shown in Figs. 6(e) and 6(f), displays a strong deviation from Eq. (11) for energies within the bias window. This signals that the electronic distribution function departs from a simple Fermi function. To highlight this aspect, in Figs. 7(b) and 7(c) we plot $\delta^{\sigma} = f(E, \mu_{\rm L}) - \bar{F}^{\sigma}_{\rm avg, MB}(E)$, where we take $f(E, \mu_{\rm L})$ [see Fig. 7(a)] as our reference equilibrium distribution, since the Co layer is much more strongly hybridized with the left-hand side lead, and $\bar{F}^{\sigma}_{\text{avg,MB}}(E)$ is the occupation of the correlated subspace averaged over the five 3dorbitals. The result shows that δ is positive for energies below $\mu_{\rm L} = eV/2$ where f = 1, whereas it becomes negative for energies above μ_L , where f = 0. This indicates that, away from equilibrium, the electronic distribution is further smeared out. In practice, electrons are excited from occupied states to higher-energy empty states, leaving behind holes. This effect becomes significant in particular for $V \gtrsim 0.4$, a threshold that coincides with the entry of the spin-up DOS peak into the bias window, and directly reflects into the calculated current, as discussed in the following section.

3. Current

The charge current as a function of bias is plotted in Fig. 8(a). The DFT and DMFT results (blue and red lines) coincide at low V but begin to diverge for $V \gtrsim 0.4$. Although the deviation remains relatively small, the underlying transport mechanisms differ fundamentally. In DFT the current is fully coherent, whereas in DMFT the incoherent contribution (black line) increasingly dominates with bias, particularly in the spin down channel.

The DFT current, obtained from the Landauer-Büttiker formula [Eq. (59)] as the integral of the transmission coefficient over the bias window, increases linearly with V, since T(E) is smooth and nearly constant across a wide energy range (see Fig. 5). In the spin-up channel, transport is dominated by delocalized 4s states, which give a large transmission. In contrast, the 3d-Co states lie well below the bias window for all V considered, as seen in the PDOS in Figs. 5(b) and 5(c), and thus they are irrelevant for transport. In the spin-down channel, the 3d-Co states play instead a more important role as they are located at energies near $E_{\rm F}$. However, their strong hybridization with the Cu left-hand side electrode causes a substantial spectral broadening, yielding a transmission coefficient that is equally large in magni-

tude and smooth in energy. Interestingly, this leads to spin-up and spin-down currents, which are nearly identical: namely, within the DFT picture, a single Co layer cannot spin-polarize the current in our set-up.

When the calculation is performed at the DMFT level, the coherent current (green line in Fig. 8) dominates at low bias and, as in DFT, increases linearly with V. At higher bias, however, it saturates, plateauing around 0.6 V, while the incoherent current rises sharply. This results in a crossover between coherent and incoherent transport at $V \sim 0.7$ V. Furthermore, the crossover is accompanied by the emergence of a negative spin current, $I^z = I^{\uparrow} - I^{\downarrow}$ [see Fig. 8(d)], indicating that bias-driven correlation effects induce spin-filtering.

The behavior of the DMFT coherent current arises from the reshaping of the transmission coefficient due to dynamical correlations [Fig. 5], most notably the \sim 0.8 eV upward shift of the spin-up 3d states, which brings them into the bias window already at \sim 0.4 V. At the same time, the transmission through the Co 3d states is suppressed relative to the DFT result because of the damping and coherence loss of the electronic excitations (see the red curves in the bottom panels of Fig. 5). This effect is encoded in the imaginary part of the DMFT self-

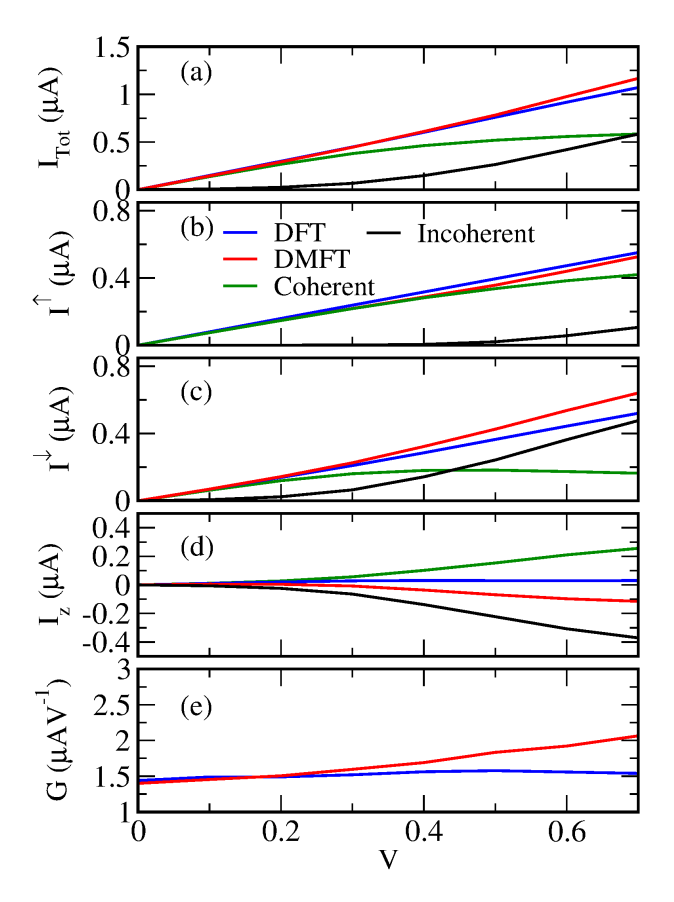


FIG. 8. (a) Total, (b) spin up, (c) spin down, (d) spin current and (e) conductance within DFT and DMFT, decomposed into its coherent and incoherent contributions, as functions of the bias.

energy. As V increases and the system is driven further away from equilibrium and from a Fermi-liquid behavior, this suppression counterbalances the widening of the bias window, and eventually results in the coherent current plateau. The effect is stronger in the spin-down channel, where 3d states lie in the bias window even at low V, whereas the spin-up channel contributes only once the bias exceeds ~ 0.4 V.

At a microscopic level, the suppression of coherent transport originates from bias-driven inelastic scattering processes, which conversely generate incoherent current. An electron entering the Co layer from the right-hand side lead can scatter off another electron, creating an electron-hole pair excitation and transferring part of its energy, before being collected in an empty state of the right-hand side lead. The electron-hole pair excitations directly manifest in the non-equilibrium distribution function as already observed in Fig. 7. Scattering between electrons of opposite spin occurs with the full interaction strength U, whereas same-spin scattering is weaker, occurring with an effective interaction U-J < U, reduced because of the Hund's coupling. As a result, opposite-spin scattering processes dominate and produce

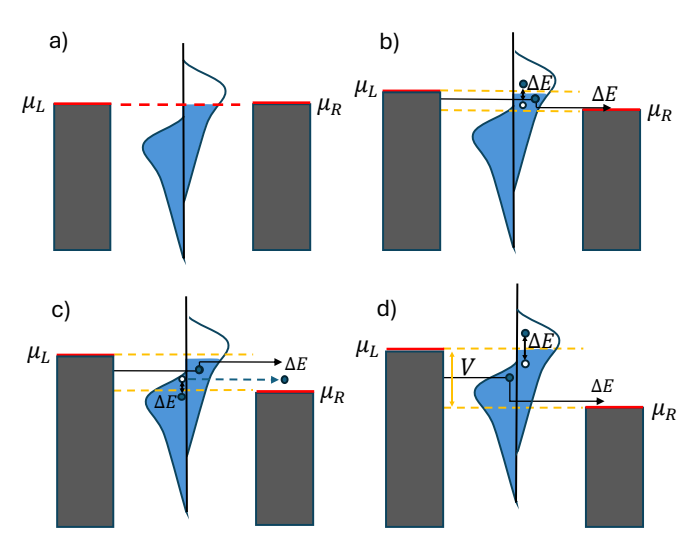


FIG. 9. Dominant scattering processes contributing to the incoherent current. Dark gray rectangles represent the Fermi boxes of the L and R leads, displaced by $\mu_L - \mu_R = V$, with the schematic Co 3d PDOS shown in between. The bias window is delimited by yellow dashed lines. Electrons (holes) are represented as filled (empty) circles. (a) Zero-bias energy-level alignment. (b) A spin-down electron creates a spin-down electron-hole pair excitation and scatters into the right lead. (c) As the bias V increases and the spin-up 3d states approach the bias window, virtual transfer of spin-up electrons into the right lead becomes possible (dashed blue arrow), leaving behind spin-up particle-hole pairs that can scatter with spindown electrons. (d) Once the bias window is large enough to include a significant portion of the spin-up PDOS, spin-up electrons contribute directly to incoherent transport by exciting opposite- (or same-) spin electron-hole pairs and scattering inelastically into the right lead.

the strongest effect on transport.

Several scattering processes can be specifically identified, as shown in Fig. 9. A spin-down electron can create a spin-down electron-hole pair excitation [panel (b)]. Since the spin-down 3d states span the Fermi level, this process can occur even at low bias, resulting in a nonzero spin-down incoherent current already at small voltages, as seen in Fig. 8(c). As V increases and the spin-up 3d states enter the bias window (approximately 0.35 eV), virtual transfer of spin-up electrons into the right lead becomes possible, leaving behind spin-up particle-hole pairs that can scatter with spin-down electrons [panel (c) in Fig. 9. Since this process involves opposite-spin interactions, it is stronger and leads to the sharper upturn in the spin-down incoherent current at $V \sim 0.3 \text{ V}$ seen in Fig. 8(c). Finally, at higher bias $(V \gtrsim 0.4 \text{ V})$, once many spin-up states become available inside bias window, spin-up electrons likewise start contributing to incoherent transport by transferring energy to generate electron-hole pair excitations of both same and opposite spin [panel (d) in Fig. 9]. This is reflected in the rise of the spin-up incoherent current in Fig. 8(b).

Notably, the incoherent current contribution gives an increase in the differential conductance, dI/dV at $V \sim 0.25$ eV. This feature is consistent with STS measurements at positive bias on Co, though observed not in extended layers but at the centers of Co nanoislands on Cu [129, 130]. While STS results are often interpreted in terms of coherent transport through the spin-up 3d Co bands within a DFT-based Tersoff-Hamann picture [131], our results indicate that this interpretation is incomplete. DMFT is crucial both to correctly position the spin-up 3d states, as DFT places them too low in energy, and to capture the relevant scattering processes.

While such processes have been included within the NEGF formalism for s-d exchange models [132, 133] and in ab initio approaches combining NEGF with time-dependent DFT for describing magnetic adatoms [134, 135], they are usually neglected for surfaces. Our calculations demonstrate how these limitations can be overcome.

In summary, our analysis demonstrates that non-equilibrium correlations, captured by DMFT, qualitatively change the nature of the system, reshaping its electronic structure. The crossover between coherent and incoherent contributions under bias provides a natural explanation for experimental conductance features, calling for a revision of the commonly used single-particle pictures, and highlights the importance of many-body scattering in transport through magnetic layers.

B. Fe/MgO/Fe

The second system investigated is the prototypical Fe/MgO/Fe MTJ, which is modelled here by using the same set-up as in reference [59], shown in Fig. 2. The calculations presented in Ref. [59] were based on the rigid-

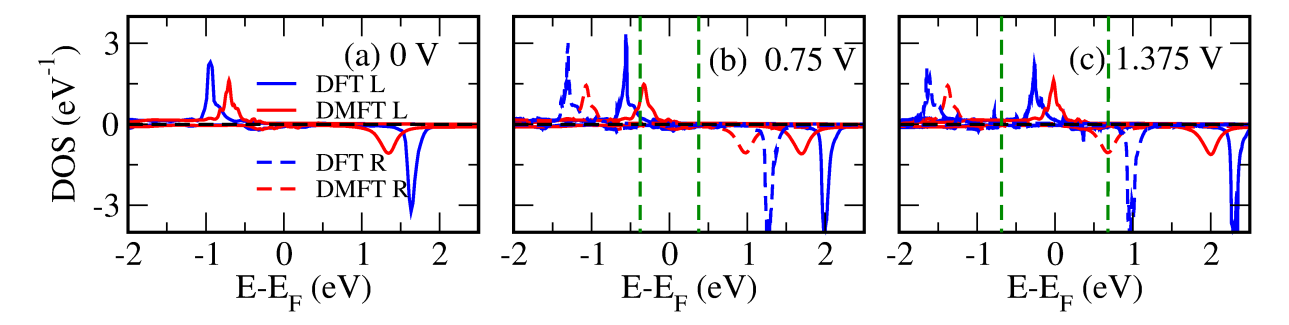


FIG. 10. The DFT and DMFT PDOS of the Δ_1 orbitals of the Fe layer to the left (L) and to the right (R) of the MgO barrier in Fe/MgO/Fe MTJ. Results are presented at (a) V = 0 V, (b) V = 0.75 V and (c) V = 1.375 V. Spin-up (down) values are shown positive (negative).

shift approximation of Sec. II D 4, which was assumed valid *a priori*. In contrast, here we perform fully non-equilibrium calculations with our improved framework to explicitly test the validity of that approximation.

The CR of our MTJ consists of three Fe layers on each side of a six-layer MgO barrier and is connected to generic simple metallic leads, which are computationally simulated as a bcc lattice of Au atoms using only the 6s orbitals as a basis set. This effectively implements a broadband approximation. The layers on the left-hand side of MgO can have a magnetization vector either parallel or antiparallel to that of the right-hand side layer, thereby realizing the two magnetic configurations of the MTJ. In this work, we focus exclusively on the parallel configuration and refer the reader to Ref. [59] for a discussion of the antiparallel case and the TMR. The correlated subspace \mathcal{C} comprises the Fe 3d orbitals, whereas the MgO barrier is treated within KS DFT, since it is weakly correlated. In fact, its conduction and valence bands have predominantly Mg-3s and O-2p character [136], respectively. The DMFT calculations use the average screened interaction parameters U = 2.0 eV and J = 0.5 eV, which were found appropriate to describe Fe nanostructures in previous studies using our implementation of DFT+DMFT [57].

1. Electronic structure at zero-bias

Tunneling through Fe/MgO/Fe MTJs is dominated by spin-split evanescent states with Δ_1 symmetry, which have the slowest decay rate inside the MgO barrier [137, 138]. Within our reference frame, where the transport direction is aligned along the z axis, and for a cubic space group, the Δ_1 states are those that transform as a linear combination of s, p_z , and d_{z^2} atomic orbitals. The zero-bias Δ_1 -PDOS of the Fe atom at the Fe/MgO interface are presented in Fig. 10(a) for DFT and DMFT, respectively. By symmetry, the results are identical for the two Fe layers at opposite side of the junction.

Within DFT, sharp spin-split peaks appear at $E-E_{\rm F}\approx -0.9$ eV and ≈ 1.6 eV for the spin-up and spin-

down channels, respectively. In contrast, DMFT yields a substantial shift in energy of these peaks, resulting in a reduction of the spin-splitting, as observed in the Cu/Co system. This is due to the real part of the self-energy, and it is accompanied by a pronounced broadening caused by the imaginary part, which vanishes at $E_{\rm F}$ as a consequence of its Fermi-liquid nature. Our results reproduce exactly those reported in Ref. [59], except for small quantitative differences in the peak positions that can be attributed to the different treatment of the double-counting correction [see discussion in Sec. II D 6]. Overall, our results provide a detailed account of correlation effects at the Fe/MgO interface.

2. Electronic structure at finite-bias

At finite bias, the electrostatic potential drops within the MgO barrier. The Fe Δ_1^{σ} state at the left-hand side Fe/MgO interface, $\Delta_{1(L)}^{\sigma}$, shifts upward in energy by +eV/2, while the corresponding state at the right-hand side, $\Delta_{1(R)}^{\sigma}$, shifts downward by -eV/2, as can be seen in Fig. 10(b) and 10(c). Differently from the Co/Cu case, where the self-energy undergoes significant changes at large bias, in the Fe/MgO/Fe MTJ the imaginary part of the self-energy [Fig. 11(c) and 11(d)] just shifts with energy, essentially retaining its Fermi-liquid character, to vanish quadratically at $\mu_{\rm L}=E_{\rm F}+eV/2$ ($\mu_{\rm R}=E_{\rm F}-eV/2$) for the Fe atoms at the left-hand (right-hand) side interface.

Since the correlated Fe atoms are strongly coupled to one lead and separated from the opposite lead by a sufficiently thick MgO barrier — so that their interaction with the latter is negligible — they can be considered in equilibrium with the lead which they are coupled to. Indeed, we find that the retarded and lesser self-energies satisfy the fluctuation-dissipation relation, Eq. (11), at all V, as shown in Fig. 11. This directly demonstrates that the rigid-shift approximation holds for this system and confirms a posteriori its application in Ref. [59]. As a result, the electronic structure at finite bias essentially follows from the zero-bias one, with genuine non-

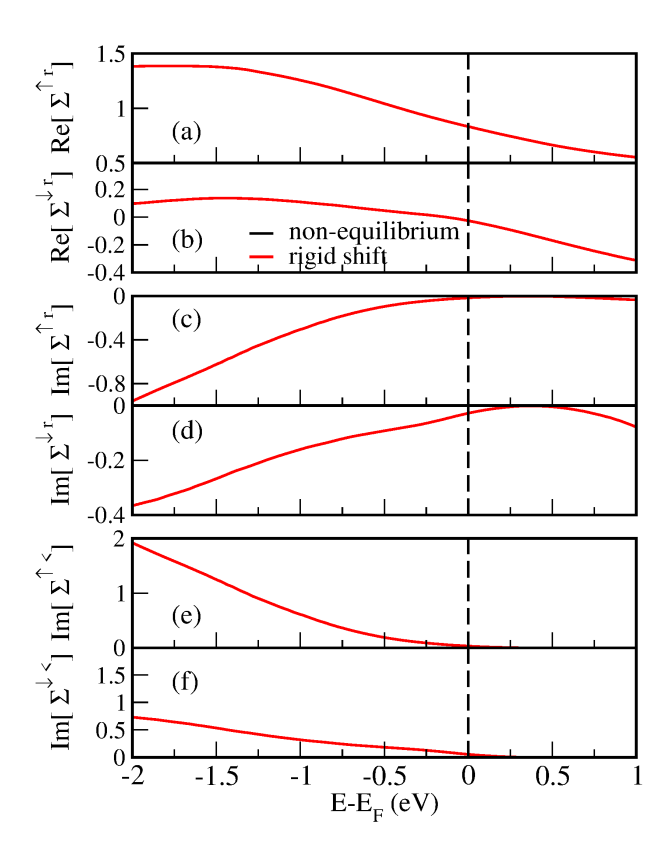


FIG. 11. Comparison of the DMFT self-energy for the Fe monolayer closest to the left-hand side of the MgO barrier. Results are averaged over all 3d orbitals, in the Fe/MgO/Fe MTJ with and without the rigid-shift approximation at V=0.75 V. Top panel: real part of the retarded component. Middle panel: imaginary part of the retarded component. Bottom panel: lesser component.

equilibrium correlation effects being negligible.

3. Current

The charge current as a function of the bias is shown in Fig. 12. At low biases, the DFT and DMFT results nearly coincide, with a fully coherent current dominated by the spin-up component, I^{\uparrow} . This is because transport is mostly through the highly conductive s states forming the Fe Δ_1 band. As the bias increases, however, the spin-up Δ_1 peak — dominated by d_{z^2} states from the left Fe layers — enters the bias window [Fig. 10(b) and 10(c), and I^{\uparrow} saturates into a plateau. The crossover from the linear regime to the plateau occurs in DMFT at a V lower than in DFT, reflecting the different energy positions of the spin-up d_{z^2} states predicted by the two methods. More interestingly, at this crossover bias, DMFT also reveals the onset of an incoherent contribution to the current, similar to what we found in the Cu/Co junction. In this case, however, the incoherent component accounts for only about 10% of the total spinup current. The underlying scattering process involves an

incoming spin-up electron interacting with electron-hole pair of the same spin, which is activated when the spin-up Δ_1 state of the left layers enters the bias window, at $V\approx 0.7~{\rm V}.$

In the spin-down channel, the current remains negligible as long as the spin-down Δ_1 state is outside the bias window. Once this state enters the window, the spin-down current suddenly increases, with the threshold in DMFT being at lower energies than in DFT. This, again, reflects the DMFT shift in the energy of the Δ_1 state.

In summary, although the applied bias has only a weak effect on Fe, bias-induced renormalization of the Δ_1 energy position and scattering from dynamical correlations remain important in Fe/MgO/Fe. This is consistent with the findings of Ref. [59], where their experimental relevance is discussed in detail. DMFT thus offers a better description than DFT, even for this technologically relevant system.

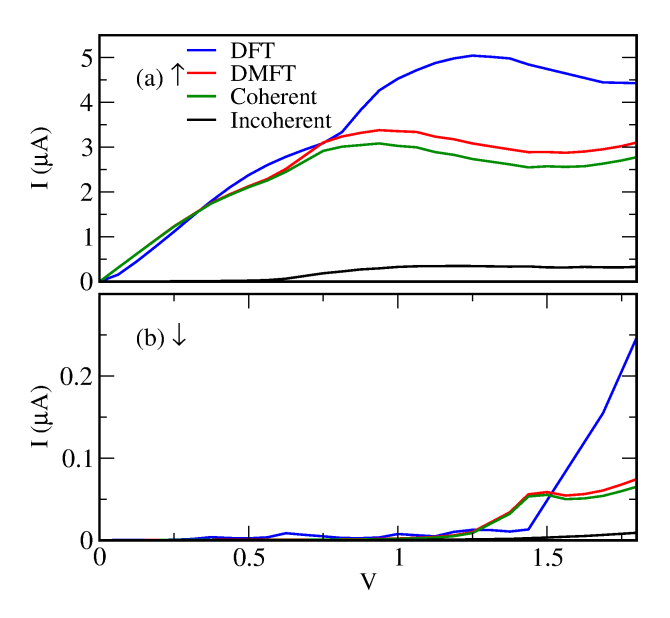


FIG. 12. Spin (a) up and (b) down currents for the Fe/MgO/Fe MTJ calculated with DFT and DMFT, and decomposed into coherent and incoherent contributions as a function of bias.

V. CONCLUSION

We have introduced a framework that combines DFT, DMFT and the NEGF method to study steady-state transport in two-terminal devices beyond the linear response, and including dynamical electron-correlation effects. By employing second-order perturbation theory as impurity solver, our approach is well suited for moderately correlated 3d transition metals. However, the method can in principle be extended to more strongly correlated materials, provided that reliable multi-orbital non-equilibrium solvers become available — an outstanding challenge at present.

As a first application, we have investigated a single Co monolayer sandwiched between Cu electrodes, where a vacuum gap is introduced at one side to enable a potential drop under bias. This is a configuration that resembles that encountered in an STM/STS experiment. Our results show that non-equilibrium dynamical correlation in Co drives a qualitative transition from Fermi-liquid to non-Fermi-liquid behavior, originating from inelastic scattering of electrons with collective electron-hole excitations. This re-shapes the electronic structure and generates incoherent contributions to the current, accompanied by a sharp increase in conductance around $V \sim 0.4 \text{ V}$, where the spin-up Co states enter the bias window. These findings provide a natural explanation for STS results, calling for a revision of commonly used single-particle models, and underscore the critical role of many-body scattering in transport through magnetic layers.

We have then applied the framework to an Fe/MgO/Fe MTJ. We find that the Fe layers remain close to equilibrium, showing that the rigid-shift approximation of Ref. [59] holds for this system. As a result, the electronic structure at finite bias essentially follows that at zero bias, with genuine non-equilibrium correlation effects being negligible. Nonetheless, we still observe the emergence of a partially incoherent current as the Fe 3d states enter the bias window, in agreement with previous results [59], demonstrating that dynamical correlation affects transport even in this technologically relevant system.

Overall, our framework provides a pathway toward modeling spintronic devices with explicit many-electron effects at finite bias in far-from-equilibrium conditions. Looking ahead, this can be generalized to compute spin currents in non-collinear and spin-orbit-coupled systems by building on the computational modules already employed in standard DFT+NEGF calculations [27, 139]. This will make it possible to study how scattering processes, such as those identified here, influence spintransfer torque [140, 141] and spin-orbit torque [142, 143], offering new insights into current-induced spin dynamics beyond the state-of-the-art *ab initio* single-particle treatment.

ACKNOWLEDGEMENTS

D.N. was supported by the Irish Research Council (Grant No. GOIPG/2021/1468). A.D. acknowledges

funding by Science Foundation Ireland (SFI) and the Royal Society through the University Research Fellowship URF/R1/191769 during the initial stage of the project, when he was employed at Trinity College Dublin. S.S. thanks Research Ireland (AMBER Center grant 12/RC/2278_P2) for support. Computational resources were provided by Trinity College Dublin Research IT.

Appendix A1: Current conservation

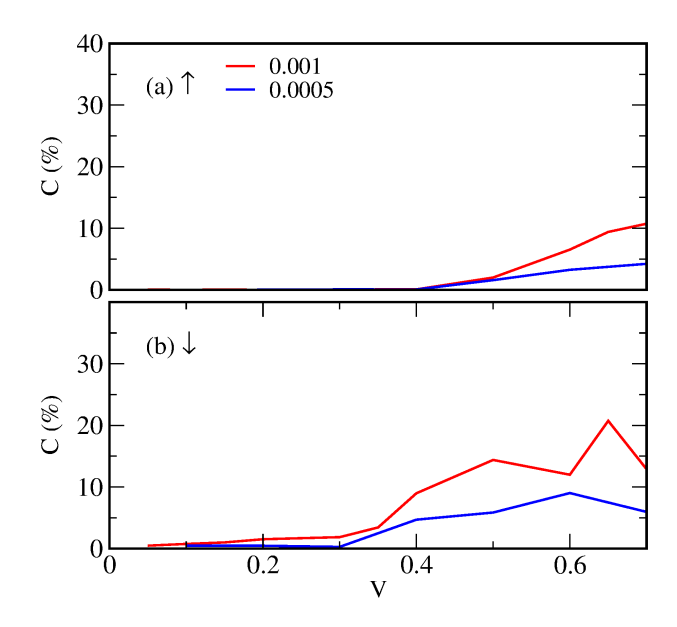


FIG. A1. The current conservation for the (a) spin up and (b) spin down channel.

Charge conservation in DFT+NEGF+DMFT is quantified as $C=100\%(2|\frac{I_{\rm L}-I_{\rm R}}{I_{\rm L}+I_{\rm R}}|)$. Figure A1 shows C for DMFT self-energies converged in the self-consistent loop to tolerances of 10^{-3} and 5×10^{-4} . Reducing the tolerance improves current conservation across the bias range. The data in Fig. 8 use the 5×10^{-4} tolerance, yielding a maximum deviation of 10%. This demonstrates that our DFT+NEGF+DMFT framework provides qualitatively — and potentially quantitatively — reliable predictions for transport in realistic heterostructures.

E. Tsymbal and I. Žutić, eds., Spintronics Handbook: Spin Transport and Magnetism (2nd ed.) (CRC Press, 2019).

^[2] M. Bowen, V. Cros, F. Petroff, A. Fert, C. Martínez Boubeta, J. L. Costa-Krämer, J. V. Anguita, A. Cebollada, F. Briones, J. M. de Teresa,

et al., Applied Physics Letters **79**, 1655 (2001), URL https://doi.org/10.1063/1.1404125.

^[3] W. H. Butler, X.-G. Zhang, T. C. Schulthess, and J. M. MacLaren, Phys. Rev. B 63, 054416 (2001), URL https://link.aps.org/doi/10.1103/PhysRevB. 63.054416.

- [4] J. Mathon and A. Umerski, Phys. Rev. B 63, 220403 (2001), URL https://link.aps.org/doi/10. 1103/PhysRevB.63.220403.
- [5] S. Yuasa, T. Nagahama, A. Fukushima, Y. Suzuki, and K. Ando, Nature Materials 3, 868 (2004), ISSN 1476-4660, URL https://doi.org/10.1038/nmat1257.
- [6] M. Julliere, Physics Letters A 54, 225 (1975), ISSN 0375-9601, URL https://www.sciencedirect. com/science/article/pii/0375960175901747.
- [7] T. Miyazaki and N. Tezuka, Journal of Magnetism and Magnetic Materials 139, L231 (1995), ISSN 0304-8853, URL https://www.sciencedirect.com/science/article/pii/0304885395900012.
- [8] J. S. Moodera, L. R. Kinder, T. M. Wong, and R. Meservey, Phys. Rev. Lett. 74, 3273 (1995), URL https://link.aps.org/doi/10.1103/PhysRevLett.74.3273.
- [9] R. O. Jones and O. Gunnarsson, Rev. Mod. Phys. 61, 689 (1989), URL http://link.aps.org/doi/10.1103/RevModPhys.61.689.
- [10] W. Kohn, Rev. Mod. Phys. 71, 1253 (1999).
- [11] R. O. Jones, Rev. Mod. Phys. 87, 897 (2015), URL http://link.aps.org/doi/10.1103/RevModPhys.87. 897
- [12] U. von Barth and L. Hedin, J. Phys. C 5, 1629 (1972).
- [13] S. H. Vosko, L. Wilk, and M. Nusair, Can. J. Phys. 58, 1200 (1980).
- [14] J. P. Perdew, J. A. Chevary, S. H. Vosko, K. A. Jackson, M. R. Pederson, D. J. Singh, and C. Fiolhais, Phys. Rev. B 46, 6671 (1992), URL https://link.aps.org/doi/ 10.1103/PhysRevB.46.6671.
- [15] J. P. Perdew, J. A. Chevary, S. H. Vosko, K. A. Jackson, M. R. Pederson, D. J. Singh, and C. Fiolhais, Phys. Rev. B 48, 4978 (1993), URL https://link.aps.org/doi/ 10.1103/PhysRevB.48.4978.2.
- [16] J. P. Perdew, K. Burke, and M. Ernzerhof, Phys. Rev. Lett. 77, 3865 (1996), URL https://link.aps.org/doi/10.1103/PhysRevLett.77.3865.
- [17] R. Landauer, IBM Journal of Research and Development 1, 223 (1957).
- [18] M. Büttiker, Phys. Rev. Lett. 57, 1761 (1986), URL https://link.aps.org/doi/10.1103/PhysRevLett. 57.1761.
- [19] M. Buttiker, IBM Journal of Research and Development 32, 317 (1988).
- [20] S. Sanvito, in Handbook of Computational Nanotechnology, Vol. 5, edited by M. Rieth and W. Schommers (American Scientific Publishers, 2005), URL https://doi.org/10.48550/arXiv.cond-mat/0503445.
- [21] D. Wortmann, H. Ishida, and S. Blügel, Phys. Rev. B 65, 165103 (2002), URL https://link.aps.org/doi/ 10.1103/PhysRevB.65.165103.
- [22] D. Wortmann, H. Ishida, and S. Blügel, Phys. Rev. B 66, 075113 (2002), URL https://link.aps.org/doi/ 10.1103/PhysRevB.66.075113.
- [23] J. M. MacLaren, X.-G. Zhang, W. H. Butler, and X. Wang, Phys. Rev. B 59, 5470 (1999), URL https: //link.aps.org/doi/10.1103/PhysRevB.59.5470.
- [24] P. A. Khomyakov, G. Brocks, V. Karpan, M. Zwierzycki, and P. J. Kelly, Phys. Rev. B 72, 035450 (2005), URL https://link.aps.org/doi/10.1103/PhysRevB. 72.035450.
- [25] G. Stefanucci and R. van Leeuwen, Nonequilibrium Many-Body Theory of Quantum Systems: A Modern Introduction (Cambridge University Press, 2013).

- [26] S. Datta, Electronic Transport in Mesoscopic Systems (Cambridge University Press, 1995).
- [27] I. Rungger, A. Droghetti, and M. Stamenova, in Handbook of Materials Modeling. Vol. 1 Methods: Theory and Modeling, edited by S. Yip and W. W. Andreoni (Springer International Publishing, 2019).
- [28] J. Taylor, H. Guo, and J. Wang, Phys. Rev. B 63, 245407 (2001), URL https://link.aps.org/doi/10. 1103/PhysRevB.63.245407.
- [29] M. Brandbyge, J.-L. Mozos, P. Ordejón, J. Taylor, and K. Stokbro, Phys. Rev. B 65, 165401 (2002), URL https://link.aps.org/doi/10.1103/PhysRevB. 65.165401.
- [30] A. R. Rocha, V. M. García-Suárez, S. Bailey, C. Lambert, J. Ferrer, and S. Sanvito, Phys. Rev. B 73, 085414 (2006), URL https://link.aps.org/doi/10.1103/PhysRevB.73.085414.
- [31] I. Rungger, O. Mryasov, and S. Sanvito, Phys. Rev. B 79, 094414 (2009), URL https://link.aps.org/doi/ 10.1103/PhysRevB.79.094414.
- [32] N. M. Caffrey, T. Archer, I. Rungger, and S. Sanvito, Phys. Rev. B 83, 125409 (2011), URL https://link. aps.org/doi/10.1103/PhysRevB.83.125409.
- [33] K. K. Saha, A. Blom, K. S. Thygesen, and B. K. Nikolić, Phys. Rev. B 85, 184426 (2012), URL https://link. aps.org/doi/10.1103/PhysRevB.85.184426.
- [34] K. Dolui, A. Narayan, I. Rungger, and S. Sanvito, Phys. Rev. B 90, 041401 (2014), URL https://link.aps. org/doi/10.1103/PhysRevB.90.041401.
- [35] P. Martin, B. Dlubak, R. Mattana, P. Seneor, M.-B. Martin, T. Henner, F. Godel, A. Sander, S. Collin, L. Chen, et al., Nanoscale 14, 12692 (2022), URL http://dx.doi.org/10.1039/D2NR01917E.
- [36] J. Slonczewski, Journal of Magnetism and Magnetic Materials 159, L1 (1996), ISSN 0304-8853, URL https://www.sciencedirect.com/science/article/ pii/0304885396000625.
- [37] L. Berger, Phys. Rev. B 54, 9353 (1996), URL https: //link.aps.org/doi/10.1103/PhysRevB.54.9353.
- [38] E. B. Myers, D. C. Ralph, J. A. Katine, R. N. Louie, and R. A. Buhrman, Science 285, 867 (1999), URL https://www.science.org/doi/abs/10.1126/science.285.5429.867.
- [39] J. A. Katine, F. J. Albert, R. A. Buhrman, E. B. Myers, and D. C. Ralph, Phys. Rev. Lett. 84, 3149 (2000), URL https://link.aps.org/doi/10. 1103/PhysRevLett.84.3149.
- [40] S. Kurth and G. Stefanucci, Journal of Physics: Condensed Matter 29, 413002 (2017), URL https://dx. doi.org/10.1088/1361-648X/aa7e36.
- [41] S. Monastra, F. Manghi, C. A. Rozzi, C. Arcangeli, E. Wetli, H.-J. Neff, T. Greber, and J. Osterwalder, Phys. Rev. Lett. 88, 236402 (2002), URL https:// link.aps.org/doi/10.1103/PhysRevLett.88.236402.
- [42] A. L. Walter, J. D. Riley, and O. Rader, New Journal of Physics 12, 013007 (2010), URL https://dx.doi.org/ 10.1088/1367-2630/12/1/013007.
- [43] S. Zhang, P. M. Levy, A. C. Marley, and S. S. P. Parkin, Phys. Rev. Lett. 79, 3744 (1997), URL https://link. aps.org/doi/10.1103/PhysRevLett.79.3744.
- [44] R. Matsumoto, Y. Hamada, M. Mizuguchi, M. Shiraishi, H. Maehara, K. Tsunekawa, D. D. Djayaprawira, N. Watanabe, Y. Kurosaki, T. Nagahama, et al., Solid State Communications 136, 611 (2005), ISSN

- 0038-1098, URL https://www.sciencedirect.com/science/article/pii/S0038109805008070.
- [45] L. Liu, J. Niu, L. Xiang, J. Wei, D.-L. Li, J.-F. Feng, X.-F. Han, X.-G. Zhang, and J. M. D. Coey, Phys. Rev. B 90, 195132 (2014), URL https://link.aps.org/doi/10.1103/PhysRevB.90.195132.
- [46] D. Bang, T. Nozaki, D. D. Djayaprawira, M. Shiraishi, Y. Suzuki, A. Fukushima, H. Kubota, T. Nagahama, S. Yuasa, H. Maehara, et al., Journal of Applied Physics 105, 07C924 (2009), ISSN 0021-8979, URL https://doi.org/10.1063/1.3063674.
- [47] M. Büttiker, Phys. Rev. B 32, 1846 (1985), URL https: //link.aps.org/doi/10.1103/PhysRevB.32.1846.
- [48] A. Fabian, M. Gradhand, M. Czerner, and C. Heiliger, Phys. Rev. B 105, 165106 (2022), URL https://link. aps.org/doi/10.1103/PhysRevB.105.165106.
- [49] W. Metzner and D. Vollhardt, Phys. Rev. Lett. 62, 324 (1989).
- [50] A. Georges, G. Kotliar, W. Krauth, and M. J. Rozenberg, Rev. Mod. Phys. 68, 13 (1996).
- [51] A. I. Lichtenstein and M. I. Katsnelson, Phys. Rev. B 57, 6884 (1998), URL https://link.aps.org/doi/10. 1103/PhysRevB.57.6884.
- [52] A. I. Lichtenstein, M. I. Katsnelson, and G. Kotliar, Phys. Rev. Lett. 87, 067205 (2001).
- [53] G. Kotliar and D. Vollhardt, Phys. Today 57, 53 (2004).
- [54] G. Kotliar, S. Y. Savrasov, K. Haule, V. S. Oudovenko, O. Parcollet, and C. A. Marianetti, Rev. Mod. Phys. 78, 865 (2006).
- [55] J. Braun, J. Minár, H. Ebert, M. I. Katsnelson, and A. I. Lichtenstein, Phys. Rev. Lett. 97, 227601 (2006), URL https://link.aps.org/doi/10.1103/PhysRevLett.97.227601.
- [56] A. Grechnev, I. Di Marco, M. I. Katsnelson, A. I. Lichtenstein, J. M. Wills, and O. Eriksson, Phys. Rev. B 76, 035107 (2007), URL https://link.aps.org/doi/10.1103/PhysRevB.76.035107.
- [57] A. Droghetti, M. M. Radonjić, A. Halder, I. Rungger, and L. Chioncel, Phys. Rev. B 105, 115129 (2022), URL https://link.aps.org/doi/10.1103/PhysRevB. 105.115129.
- [58] D. M. Janas, A. Droghetti, S. Ponzoni, I. Cojocariu, M. Jugovac, V. Feyer, M. M. Radonjić, I. Rungger, L. Chioncel, G. Zamborlini, et al., Advanced Materials 35, 2205698 (2023), URL https://onlinelibrary. wiley.com/doi/abs/10.1002/adma.202205698.
- [59] D. Nell, S. Sanvito, I. Rungger, and A. Droghetti, Phys. Rev. B 111, 035133 (2025), URL https://link.aps. org/doi/10.1103/PhysRevB.111.035133.
- [60] M. Potthoff and W. Nolting, Phys. Rev. B 59, 2549 (1999), URL https://link.aps.org/doi/10. 1103/PhysRevB.59.2549.
- [61] S. Okamoto and A. J. Millis, Phys. Rev. B 70, 241104 (2004), URL https://link.aps.org/doi/10. 1103/PhysRevB.70.241104.
- [62] J. K. Freericks, Phys. Rev. B 70, 195342 (2004), URL https://link.aps.org/doi/10.1103/PhysRevB. 70.195342.
- [63] T. Oka and N. Nagaosa, Phys. Rev. Lett. 95, 266403 (2005), URL https://link.aps.org/doi/10. 1103/PhysRevLett.95.266403.
- [64] S. Yunoki, A. Moreo, E. Dagotto, S. Okamoto, S. S. Kancharla, and A. Fujimori, Phys. Rev. B 76, 064532 (2007), URL https://link.aps.org/doi/10.

- 1103/PhysRevB.76.064532.
- [65] H. Zenia, J. K. Freericks, H. R. Krishnamurthy, and T. Pruschke, Phys. Rev. Lett. 103, 116402 (2009), URL https://link.aps.org/doi/10.1103/ PhysRevLett.103.116402.
- [66] A. Valli, G. Sangiovanni, O. Gunnarsson, A. Toschi, and K. Held, Phys. Rev. Lett. 104, 246402 (2010), URL https://link.aps.org/doi/10.1103/ PhysRevLett.104.246402.
- [67] A. Valli, G. Sangiovanni, A. Toschi, and K. Held, Phys. Rev. B 86, 115418 (2012), URL https://link.aps. org/doi/10.1103/PhysRevB.86.115418.
- [68] A. Droghetti, M. c. v. M. Radonjić, L. Chioncel, and I. Rungger, Phys. Rev. B 106, 075156 (2022), URL https://link.aps.org/doi/10.1103/PhysRevB. 106.075156.
- [69] L. Chioncel, C. Morari, A. Ostlin, W. H. Appelt, A. Droghetti, M. M. Radonjić, I. Rungger, L. Vitos, U. Eckern, and A. V. Postnikov, Phys. Rev. B 92, 054431 (2015), URL https://link.aps.org/doi/10. 1103/PhysRevB.92.054431.
- [70] C. Morari, W. H. Appelt, A. Östlin, A. Prinz-Zwick, U. Schwingenschlögl, U. Eckern, and L. Chioncel, Phys. Rev. B 96, 205137 (2017), URL https://link.aps. org/doi/10.1103/PhysRevB.96.205137.
- [71] A. Halder, D. Nell, A. Sihi, A. Bajaj, S. Sanvito, and A. Droghetti, Nano Letters 24, 9221 (2024), pMID: 39037057, URL https://doi.org/10.1021/ acs.nanolett.4c01479.
- [72] D. J. Abramovitch, J. Mravlje, J.-J. Zhou, A. Georges, and M. Bernardi, Phys. Rev. Lett. 133, 186501 (2024), URL https://link.aps.org/doi/10.1103/ PhysRevLett.133.186501.
- [73] D. Jacob, K. Haule, and G. Kotliar, Phys. Rev. Lett. 103, 016803 (2009), URL https://link.aps.org/doi/ 10.1103/PhysRevLett.103.016803.
- [74] D. Jacob, K. Haule, and G. Kotliar, Phys. Rev. B 82, 195115 (2010), URL https://link.aps.org/doi/10. 1103/PhysRevB.82.195115.
- [75] D. Jacob, Journal of Physics: Condensed Matter 27, 245606 (2015), URL https://doi.org/10.1088/ 0953-8984/27/24/245606.
- [76] D. Jacob, M. Soriano, and J. J. Palacios, Phys. Rev. B 88, 134417 (2013), URL https://link.aps.org/doi/ 10.1103/PhysRevB.88.134417.
- [77] A. Droghetti and I. Rungger, Phys. Rev. B 95, 085131 (2017), URL https://link.aps.org/doi/10. 1103/PhysRevB.95.085131.
- [78] W. H. Appelt, A. Droghetti, L. Chioncel, M. M. Radonjić, E. Muñoz, S. Kirchner, D. Vollhardt, and I. Rungger, Nanoscale 10, 17738 (2018), URL http://dx.doi.org/10.1039/C8NR03991G.
- [79] M. Rumetshofer, D. Bauernfeind, E. Arrigoni, and W. von der Linden, Phys. Rev. B 99, 045148 (2019), URL https://link.aps.org/doi/10.1103/PhysRevB. 99.045148.
- [80] S. Bhandary, J. M. Tomczak, and A. Valli, Nanoscale Adv. 3, 4990 (2021), URL http://dx.doi.org/10. 1039/D1NA00407G.
- [81] G. Gandus, D. Passerone, R. Stadler, M. Luisier, and A. Valli, Strongly correlated physics in organic openshell quantum systems (2022), 2301.00282, URL https: //arxiv.org/abs/2301.00282.
- [82] D. Jacob, Journal of Physics: Condensed Matter

- **30**, 354003 (2018), URL https://doi.org/10.1088/1361-648x/aad523.
- [83] H. Aoki, N. Tsuji, M. Eckstein, M. Kollar, T. Oka, and P. Werner, Reviews of Modern Physics 86, 779–837 (2014), ISSN 1539-0756, URL http://dx.doi.org/10.1103/RevModPhys.86.779.
- [84] M. Schüler, D. Golež, Y. Murakami, N. Bittner, A. Herrmann, H. U. Strand, P. Werner, and M. Eckstein, Computer Physics Communications 257, 107484 (2020), ISSN 0010-4655, URL http://dx.doi.org/10.1016/j.cpc.2020.107484.
- [85] J. Yan and P. Werner, Phys. Rev. B 108, 125143 (2023), URL https://link.aps.org/doi/10.1103/PhysRevB. 108.125143.
- [86] S. Okamoto, Phys. Rev. B 76, 035105 (2007), URL https://link.aps.org/doi/10.1103/PhysRevB. 76.035105.
- [87] S. Okamoto, Phys. Rev. Lett. 101, 116807 (2008), URL https://link.aps.org/doi/10.1103/PhysRevLett. 101.116807.
- [88] A. Erpenbeck, E. Gull, and G. Cohen, Phys. Rev. Lett. 130, 186301 (2023), URL https://link.aps.org/doi/ 10.1103/PhysRevLett.130.186301.
- [89] E. Arrigoni, M. Knap, and W. von der Linden, Phys. Rev. Lett. 110, 086403 (2013), URL https://link. aps.org/doi/10.1103/PhysRevLett.110.086403.
- [90] F. Lechermann, A. Georges, A. Poteryaev, S. Biermann, M. Posternak, A. Yamasaki, and O. K. Andersen, Phys. Rev. B 74, 125120 (2006), URL https://link.aps.org/doi/10.1103/PhysRevB.74.125120.
- [91] J. M. Soler, E. Artacho, J. D. Gale, A. García, J. Junquera, P. Ordejón, and D. Sánchez-Portal, Journal of Physics: Condensed Matter 14, 2745 (2002), URL https://doi.org/10.1088/0953-8984/14/11/302.
- [92] A. García, N. Papior, A. Akhtar, E. Artacho, V. Blum, E. Bosoni, P. Brandimarte, M. Brandbyge, J. I. Cerdá, F. Corsetti, et al., J. Chem. Phys. 152, 204108 (2020), ISSN 0021-9606, URL https://doi.org/10.1063/5. 0005077.
- [93] H. Haug and A. Jauho, Quantum Kinetics in Transport and Optics of Semiconductors, Solid-State Sciences Series (Springer Berlin Heidelberg, 1996), ISBN 9783540616023.
- [94] Y. Meir and N. S. Wingreen, Phys. Rev. Lett. 68, 2512 (1992), URL https://link.aps.org/doi/10. 1103/PhysRevLett.68.2512.
- [95] K. S. Thygesen and A. Rubio, Phys. Rev. B 77, 115333 (2008), URL https://link.aps.org/doi/10. 1103/PhysRevB.77.115333.
- [96] A. P. Jauho, Introduction to the keldysh nonequilibrium green function technique, https://materias.df.uba.ar/solidosa2012c2/files/2012/07/jauho.pdf (2006), lecture notes.
- [97] I. Rungger and S. Sanvito, Phys. Rev. B 78, 035407 (2008), URL https://link.aps.org/doi/10. 1103/PhysRevB.78.035407.
- [98] M. P. L. Sancho, J. M. L. Sancho, and J. Rubio, Journal of Physics F: Metal Physics 14, 1205 (1984), URL https://dx.doi.org/10.1088/0305-4608/14/5/016.
- [99] H. Ness, L. K. Dash, and R. W. Godby, Phys. Rev. B 82, 085426 (2010), URL https://link.aps.org/doi/ 10.1103/PhysRevB.82.085426.
- [100] K. S. Thygesen and A. Rubio, The Journal of Chemical Physics **126**, 091101 (2007), ISSN

- 0021-9606, https://pubs.aip.org/aip/jcp/article-pdf/doi/10.1063/1.2565690/13381330/091101_1_online.pdf, URL https://doi.org/10.1063/1.2565690.
- [101] A. Ferretti, A. Calzolari, R. Di Felice, and F. Manghi, Phys. Rev. B 72, 125114 (2005), URL https://link. aps.org/doi/10.1103/PhysRevB.72.125114.
- [102] A. Ferretti, A. Calzolari, R. Di Felice, F. Manghi, M. J. Caldas, M. B. Nardelli, and E. Molinari, Phys. Rev. Lett. 94, 116802 (2005), URL https://link.aps.org/doi/10.1103/PhysRevLett.94.116802.
- [103] L. Deuschle, J. Cao, A. N. Ziogas, A. Winka, A. Maeder, N. Vetsch, and M. Luisier, arXiv preprint arXiv:2412.12986 (2024), 2412.12986, URL https:// arxiv.org/abs/2412.12986.
- [104] I. Rungger, Ph.D. thesis, Trinity College (Dublin, Ireland). School of Physics, (2009).
- [105] R. Zeller, in Magnetism, in Computational Nanoscience: Do It Yourself!, edited by J. Grotendorst, S. Blügel, and D. Marx (NIC Serie, Forschungszentrum Julich, 2006), http://juser.fz-juelich.de/record/54009/files/FZJ-2014-02225.pdf.
- [106] E. Pavarini, in The LDA+DMFT approach to strongly correlated materials Modeling and Simulation Vol. 1, edited by E. Pavarini, E. Koch, D. Vollhardt, and A. Lichtenstein (Forschungszentrum Julich, 2011).
- [107] M. Karolak, G. Ulm, T. Wehling, V. Mazurenko, A. Poteryaev, and A. Lichtenstein, Journal of Electron Spectroscopy and Related Phenomena 181, 11 (2010), ISSN 0368-2048, URL https://www.sciencedirect. com/science/article/pii/S0368204810001222.
- [108] K. Haule, C.-H. Yee, and K. Kim, Phys. Rev. B 81, 195107 (2010), URL https://link.aps.org/doi/10. 1103/PhysRevB.81.195107.
- [109] E. Gull, A. J. Millis, A. I. Lichtenstein, A. N. Rubtsov, M. Troyer, and P. Werner, Rev. Mod. Phys. 83, 349 (2011), URL https://link.aps.org/doi/10.1103/RevModPhys.83.349.
- [110] M. Jarrell and J. Gubernatis, Physics Reports 269, 133 (1996), ISSN 0370-1573, URL https://www.sciencedirect.com/science/article/pii/0370157395000747.
- [111] L. Mühlbacher and E. Rabani, Phys. Rev. Lett. 100, 176403 (2008), URL https://link.aps.org/doi/10. 1103/PhysRevLett.100.176403.
- [112] T. L. Schmidt, P. Werner, L. Mühlbacher, and A. Komnik, Phys. Rev. B 78, 235110 (2008), URL https://link.aps.org/doi/10.1103/PhysRevB.78.235110.
- [113] M. Schiró and M. Fabrizio, Phys. Rev. B 79, 153302 (2009), URL https://link.aps.org/doi/10. 1103/PhysRevB.79.153302.
- [114] P. Werner, T. Oka, and A. J. Millis, Phys. Rev. B 79, 035320 (2009), URL https://link.aps.org/doi/ 10.1103/PhysRevB.79.035320.
- [115] P. Werner, T. Oka, and A. J. Millis, Phys. Rev. B 79, 035320 (2009), URL https://link.aps.org/doi/ 10.1103/PhysRevB.79.035320.
- [116] G. Steffanucci, in Simulating Correlations with Computers, edited by A. L. E. Pavarini, E. Koch, and D. Vollhardt (Forschungszentrum Jülich GmbH, Institute for Advanced Simulation, Jülich, 2021), Lecture Notes of the Autumn School on Correlated Electrons 2021, pp. 232–260.
- [117] D. M. Janas, Adv Mater 35 (2023), URL https://doi. org/10.1002/adma.202205698.

- [118] K. Held, I. A. Nekrasov, N. Blümer, V. I. Anisimov, and D. Vollhardt, International Journal of Modern Physics B 15, 2611–2625 (2001), ISSN 1793-6578, URL http: //dx.doi.org/10.1142/S0217979201006495.
- [119] S. L. Dudarev, G. A. Botton, S. Y. Savrasov, C. J. Humphreys, and A. P. Sutton, Phys. Rev. B 57, 1505 (1998), URL https://link.aps.org/doi/10. 1103/PhysRevB.57.1505.
- [120] K. S. Thygesen, Phys. Rev. B 73, 035309 (2006), URL https://link.aps.org/doi/10.1103/PhysRevB. 73.035309.
- [121] Note1, note that in Eq. (45) of Ref. [120], the Meir-Wingreen formula is recovered for a non-orthogonal basis in terms of what the author calls the "overlap Green's functions", denoted using Gothic symbols. The definition of these Green's functions in Eq. (16) of Ref. [120] coincides with the one we use in Eq. (1) so that that the application of the Meir-Wingreen formula in our work is rigorous.
- [122] M. Pickem, E. Maggio, and J. M. Tomczak, Phys. Rev. B 105, 085139 (2022), URL https://link.aps.org/doi/10.1103/PhysRevB.105.085139.
- [123] M. Kilgour and D. Segal, The Journal of Chemical Physics 143, 024111 (2015), ISSN 0021-9606, URL https://doi.org/10.1063/1.4926395.
- [124] N. Troullier and J. L. Martins, Phys. Rev. B 43, 1993 (1991), URL https://link.aps.org/doi/10. 1103/PhysRevB.43.1993.
- [125] A. V. Rudnev, V. Kaliginedi, A. Droghetti, H. Ozawa, A. Kuzume, M. aki Haga, P. Broekmann, and I. Rungger, Science Advances 3, e1602297 (2017), URL https://www.science.org/doi/abs/10.1126/sciadv. 1602297.
- [126] M. Imada, A. Fujimori, and Y. Tokura, Rev. Mod. Phys. 70, 1039 (1998).
- [127] V. I. Anisimov and O. Gunnarsson, Phys. Rev. B 43, 7570 (1991), URL https://link.aps.org/doi/10. 1103/PhysRevB.43.7570.
- [128] A. Droghetti and I. Rungger, Phys. Chem. Chem. Phys. 22, 1466 (2020), URL http://dx.doi.org/10.1039/ C9CP05474J.
- [129] M. V. Rastei, B. Heinrich, L. Limot, P. A. Ignatiev, V. S. Stepanyuk, P. Bruno, and J. P. Bucher, Phys. Rev. Lett. 99, 246102 (2007), URL https://link.aps. org/doi/10.1103/PhysRevLett.99.246102.
- [130] J. Park, C. Park, M. Yoon, and A.-P. Li, Nano Letters 17, 292 (2017), pMID: 28073266, URL https://doi. org/10.1021/acs.nanolett.6b04062.

- [131] J. Tersoff and D. R. Hamann, Phys. Rev. B 31, 805 (1985), URL https://link.aps.org/doi/10.1103/PhysRevB.31.805.
- [132] A. Hurley, N. Baadji, and S. Sanvito, Phys. Rev. B 84, 035427 (2011), URL https://link.aps.org/doi/ 10.1103/PhysRevB.84.035427.
- [133] F. Mahfouzi and B. K. Nikolić, Phys. Rev. B 90, 045115 (2014), URL https://link.aps.org/doi/10. 1103/PhysRevB.90.045115.
- [134] S. Lounis, A. T. Costa, R. B. Muniz, and D. L. Mills, Phys. Rev. Lett. 105, 187205 (2010), URL https://link.aps.org/doi/10.1103/PhysRevLett. 105.187205.
- [135] B. Schweflinghaus, M. dos Santos Dias, A. T. Costa, and S. Lounis, Phys. Rev. B 89, 235439 (2014), URL https: //link.aps.org/doi/10.1103/PhysRevB.89.235439.
- [136] F. Aryasetiawan, Phys. Rev. B 46, 13051 (1992), URL https://link.aps.org/doi/10.1103/PhysRevB. 46.13051.
- [137] W. H. Butler, X.-G. Zhang, T. C. Schulthess, and J. M. MacLaren, Phys. Rev. B 63, 054416 (2001), URL https://link.aps.org/doi/10.1103/PhysRevB. 63.054416.
- [138] W. H. Butler, Science and Technology of Advanced Materials 9, 014106 (2008), pMID: 27877932, https://doi.org/10.1088/1468-6996/9/1/014106, URL https://doi.org/10.1088/1468-6996/9/1/014106.
- [139] A. Bajaj, R. Gupta, I. V. Tokatly, S. Sanvito, and A. Droghetti, Phys. Rev. B 109, 195132 (2024), URL https://link.aps.org/doi/10.1103/PhysRevB. 109.195132.
- [140] J. Slonczewski, Journal of Magnetism and Magnetic Materials 159, L1 (1996), ISSN 0304-8853, URL https://www.sciencedirect.com/science/article/ pii/0304885396000625.
- [141] L. Berger, Phys. Rev. B 54, 9353 (1996), URL https: //link.aps.org/doi/10.1103/PhysRevB.54.9353.
- [142] I. M. Miron, K. Garello, G. Gaudin, P.-J. Zermatten, M. V. Costache, S. Auffret, S. Bandiera, B. Rodmacq, A. Schuhl, and P. Gambardella, Nature 476, 189 (2011), ISSN 1476-4687, URL https://doi.org/10.1038/nature10309.
- [143] L. Liu, C.-F. Pai, Y. Li, H. W. Tseng, D. C. Ralph, and R. A. Buhrman, Science 336, 555 (2012), URL https://www.science.org/doi/abs/10. 1126/science.1218197.